Available online at www.sciencedirect.com

ScienceDirect

Geochimica et Cosmochimica Acta 303 (2021) 15–37

Geochimica et Cosmochimica Acta

www.elsevier.com/locate/gca

Testing hypotheses of albite dissolution mechanisms at near-equilibrium using Si isotope tracers

Chen Zhu [a,*], Yilun Zhang [a,b,1], J. Donald Rimstidt [d,3], Lei Gong [a], Joseph A.C. Burkhart [a,2], Kaiyun Chen [c], Honglin Yuan [c]

[a] Department of Earth and Atmospheric Sciences, Indiana University, Bloomington, IN 47405, USA
[b] Doctoral Program in Environmental Sciences, Indiana University, Bloomington, IN 47405, USA
[c] State Key Laboratory of Continental Dynamics, Department of Geology, Northwest University, Xi'an 710069, China
[d] Department of Geosciences, Virginia Tech, Blacksburg, VA 24061, USA

Received 4 December 2020; accepted in revised form 23 March 2021; Available online 31 March 2021

Abstract

Here, we demonstrate the potential advantages of using isotope tracers to test hypotheses of reaction mechanisms near-equilibrium. Using non-traditional stable Si isotopes as tracers, we measured albite unidirectional dissolution rates (r_+) across a range of Gibbs free energy of reaction ($\Delta_r G$) close to equilibrium (−26 to −2 kJ/mol). Thirteen batch experiment series were conducted at 50 °C and pH ~ 8 ± 0.25. Different distances from equilibrium were achieved by a stepwise increase of concentrations of Si (0–600 μM), Al (0–10 μM), and Na (0–1000 μM). The temperature, pH, sample preparation, and reaction duration were kept identical to isolate the $\Delta_r G$ effect. Secondary phase precipitation, which is difficult to avoid in near-equilibrium, near-neutral pH experiments renders the rate measurement method based on changes in Si and Al concentration unworkable, but it should not impact the Si isotope ratios-based rates.

The resulting r_+ values were nearly constant in the experimental $\Delta_r G$ range, signaling no major $\Delta_r G$-related switch of reaction mechanisms. Our results suggest that the switch from etch pit opening at far-from-equilibrium to step retreat at near-equilibrium does not operate under circum-neutral pH in low-temperature systems; this mechanism switch was proposed based on experimental data in alkaline solutions at hydrothermal temperatures. The nearly constant r_+ values at pH 5–8 also suggest that an H_2O-catalyzed reaction mechanism dominant at circumneutral pH, in addition to the H^+- and OH^--catalyzed reaction mechanisms dominant at acidic and alkaline pH, respectively.

The experimental results have implications for geochemical modeling of low-temperature geological and environmental processes. The results suggest that a term of H_2O-catalyzed reaction mechanism should be included in rate laws and that the parallel rate law with a mechanism-switch is not applicable in the pH range of 5–8.

Keywords: Kinetics; Feldspar; Isotope doping; Near-equilibrium; Weathering; Carbon sequestration

1. INTRODUCTION

The question of whether mineral dissolution mechanisms change when solution chemistry shifts from far-from-equilibrium to near-equilibrium with respect to the mineral of interest is critical to geochemistry. Almost all rates measured in laboratory experiments are at far-from-

* Corresponding author.
E-mail address: chenzhu@indiana.edu (C. Zhu).
[1] Now at: Intertek Environmental Services Shenzhen, 4012 N Wuhe Ave, Longgang District, Shenzhen, Guangdong, China.
[2] Now at: The University of British Columbia, Vancouver, BC V6T 1Z1, USA
[3] Author passed away on March 24, 2019.

https://doi.org/10.1016/j.gca.2021.03.023
0016-7037/

equilibrium while the majority of natural water in aquifers, soil systems, and geothermal systems is near equilibrium with respect to minerals (Drever, 1988; McBride, 1994; White and Brantley, 1995; Langmuir, 1997). Therefore, extrapolation from far-from-equilibrium to near-equilibrium conditions is necessary to translate laboratory experimental data to models of geological and environmental processes. If reaction mechanisms change from far-from-equilibrium to near-equilibrium conditions, it would be a challenge to utilize the far-from-equilibrium rate constants (e.g., compilations by Palandri and Kharaka, 2004; Marini, 2007; Brantley et al., 2008; Marty et al., 2015; Zhang et al., 2019) and apply them to near-equilibrium field conditions.

Enduring debates and controversies surround the appropriate rate laws to extrapolate from far-from-equilibrium data to near-equilibrium rates for feldspars. At the root of the controversy is the experimental challenge of measuring near-equilibrium silicate rates and the consequent paucity of experimental data (Lüttge, 2006; Arvidson and Luttge, 2010; Schott et al., 2012; Zhu et al., 2016; Zhu et al., 2020). Laboratory experiments have relied mostly on Si (and occasionally Al) concentration changes over time to calculate reaction rates (termed *the concentration-based method* hereafter). However, because silicate reactions are slow, the concentration changes are small, which means that it is difficult to detect the changes, which may be smaller than the analytical uncertainties in the experiments (Ganor et al., 2007). If Al or Si-containing secondary phases precipitate, the Si concentrations can give misleading dissolution rates that are smaller than the actual dissolution rates.

In the past three and half decades, some near-equilibrium experiments using the concentration-based method have shown no mechanism switch (Gautier et al., 1994; Oelkers et al., 1994; Oelkers and Schott, 1995). In interpreting their experimental data, these authors have combined Transition State Theory (TST) (for the relationship between reaction rates and Gibbs free energy of reaction ($\Delta_r G$)) and surface complexation model (for the breakdown of an activated surface complex). Other authors have found in their experiments a reduction of up to two orders of magnitude in dissolution rates at near-equilibrium compared to the far-from-equilibrium rates, which they attributed to a switch of reaction mechanisms between different levels of undersaturation (Burch et al., 1993; Taylor et al., 2000; Beig and Lüttge, 2006; Hellmann and Tisserand, 2006; Lüttge, 2006; Gruber et al., 2014; Pollet-Villard et al., 2016). Burch et al. (1993), Luttge (2006), and Dove et al. (2005) suggested a switch of mechanisms at a critical Gibbs free energy of reactions, $\Delta_r G_{crit}$. When the reaction is near equilibrium ($\Delta_r G > \Delta_r G_{crit}$), the thermodynamic driving force is not large enough to open (new) etch pits at screw dislocations. Dissolution proceeds slowly during step retreat. When the reaction is far-from-equilibrium ($\Delta_r G < \Delta_r G_{crit}$), the thermodynamic driving force is strong enough to overcome the activation energy barrier to open a "hollow core" at screw dislocations into etch pits. Dissolution is 1.5 to 2 orders of magnitude faster because more active surface sites are available for reaction. Such an explanation of the mechanism switch has been rationalized from the BCF classical crystal growth theory and dissolution stepwave models (Dove et al., 2005; Luttge et al., 2019).

These controversies are far from being settled. Numerous reactive transport models of weathering, geological carbon sequestration, nuclear waste disposal, and diagenesis have used either the one-mechanism or two-mechanism rate laws for feldspars as ad hoc extrapolation from far-from-equilibrium rate constants to near-equilibrium ones. Some of these applications have societal relevance, e.g., geological carbon sequestration and nuclear waste disposal permit applications. A better scientific foundation for these applications is urgently needed.

To meet this challenge, we used non-traditional Si stable isotopes as tracers in feldspar dissolution experiments that covered a range of $\Delta_r G$ values near-equilibrium. Feldspar was chosen for this study because it is the most abundant minerals in the Earth's crust, and the kinetics of its weathering reactions is critical to understanding many geological and environmental processes, such as the release of nutrients from rocks (Bennett et al., 2001), global geochemical cycles (Lasaga et al., 1994), high-level waste disposal, and geological carbon sequestration (Zhu et al., 2015). Albite is also the mineral that has attracted most previous studies of rate dependence on $\Delta_r G$ (Burch et al., 1993; Oelkers et al., 1994; Alekseyev et al., 1997; Berger et al., 2002; Alekseyev et al., 2004; Beig and Lüttge, 2006; Hellmann and Tisserand, 2006; Zhu et al., 2010; Pollet-Villard et al., 2016).

The Si isotope tracer method used in this study is potentially a game-changer because rates based on isotope ratios are unidirectional and free from the artifact of secondary phase precipitation (Gruber et al., 2013; Zhu et al., 2016; Zhu et al., 2020). The isotope tracer technique introduces an enriched rare isotope of an element to an experimental solution that is interacting with a mineral or a suite of minerals that have normal or natural isotopic compositions (modified from Gaillardet, 2008). Si is a part of the silicate framework and Si isotopes are particularly useful to derive silicate reaction rates. This method has been successfully applied to measuring the dissolution reaction rates of albite at far-from-equilibrium (Gruber et al., 2014; Zhu et al., 2016), dissolution and precipitation reaction rates of quartz at equilibrium (Liu et al., 2016), dissolution rates of kaolinite at near-equilibrium conditions (Gong et al., 2019), and dissolution rates of albite and K-feldspar at near-equilibrium (Zhu et al., 2020).

In this study, we used the isotope tracer method and conducted 13 batch experiments of albite dissolution at 50 °C and pH ~ 8 at different levels of $\Delta_r G$. The objective is to obtain unidirectional dissolution rates, r_+, when the near-equilibrium solutions are unavoidably supersaturated with many secondary phases (see more in the next section). Our goal was not to argue that our measured rates are the best; rather, we wanted to decipher whether r_+ varies with different levels of $\Delta_r G$ in an experimental series with identical environmental conditions (sample preparation, pH, temperature, experimental duration). Numerous studies have documented discrepancies in measured albite rates of up to two orders of magnitude, resulting from differences in reaction duration and sample preparation (Fischer et al.,

2012). Our experiments used the same batch of prepared albite grains and used the same reaction duration.

The experimental approach and conditions in this study are similar to those in Zhu et al. (2020). However, Zhu et al. (2020) obtained albite dissolution rates at only a single $\Delta_r G$ point close to equilibrium ($\Delta_r G \sim 0$); this study obtained albite dissolution rates in a range of $\Delta_r G$, which allows us to test a number of near-equilibrium reaction hypotheses.

2. BACKGROUND AND HYPOTHESIS TESTING

Here, we want to establish that the rate data obtained in this study are fundamentally different from the experimental data obtained from the concentration-based method cited above. The materials below have mostly been described before in Zhu et al. (2016, 2020), but we repeat them here for the sake of clarity. For convenience, we follow the convention that *near-equilibrium* is defined as the region of $\Delta_r G/RT > -5$ (Burch et al., 1993; Rimstidt, 2014) where R denotes the gas constant and T temperature in Kelvin. At $\Delta_r G/RT = -5$, rates start to decrease with increasing $\Delta_r G$ according to the Transition State Theory (TST) rate law. In other words, the rate plateau according to the TST rate law ends. We use the expression of $\Delta_r G/RT$ to normalize experimental data at different temperatures. *Far-from-equilibrium* denotes the region $\Delta_r G/RT < -5$.

Here $\Delta_r G$ stands for Gibbs free energy of reaction, for example:

$$NaAlSi_3O_8 + 8H_2O \underset{r_-}{\overset{r_+}{\longleftrightarrow}} Na^+ + Al(OH)_4^- + 3H_4SiO_4^o(aq) \quad (1)$$

Most reported rates of silicate mineral dissolution are based on Si flux:

$$r_{net} = r_+ - r_- = \frac{1}{v \cdot S_A}\frac{d[Si]}{dt} \quad (2)$$

See Table 1 for notations and definitions. In this paper, when the term "dissolution rate" is used, it refers to r_+. "Net dissolution rate" is r_{net} when it is positive. Similarly, "precipitation rate" describes the unidirectional reaction from right to left in Reaction (1). "Net precipitation rate" is r_{net} when it is negative.

Previous studies of albite near-equilibrium reaction mechanisms relied on r_{net} data, which were almost all based on changes in [Si]. The r_{net} values were then used to evalu-

Table 1
List of symbols and definitions.

Symbol	Definition
$\Delta_r G_j$	Gibbs free energy of the jth reaction (kJ/mol)
$\Delta_f G^o$	The standard Gibbs free energy of formation (kJ mol^{-1})
f_{28}	^{28}Si fractional abundance (0 to 1) in experimental solution $f_{28} = [^{28}Si]/([^{28}Si]+[^{29}Si]+[^{30}Si])$; $f_{28} = \frac{1}{1+R_{29/28}+R_{30/28}}$; $R_{29/28}$ stands for the isotopic ratio; similarly for f_{29} and f_{30}
k_+	Apparent dissolution rate constant of albite dissolution in mol (feldspar) m^{-2} s^{-1}
k_-	Apparent precipitation rate constant of albite dissolution in mol (feldspar) m^{-2} s^{-1}
K	Equilibrium constant
R	Gas constant (8.314 J mol^{-1} K^{-1})
r_{net} $r_\pm$	The net or overall reaction rate in mol (feldspar) m^{-2} s^{-1};$r_{net} = r_+ - r_-$
r_{net}	Apparent net rate in mol (feldspar) m^{-2} s^{-1}. $r_{net} = r_+ - r_- - r_{2nd}$
r_+	The dissolution rate of feldspar dissolution in mol (feldspar) m^{-2} s^{-1}
r'_+	The dissolution rate of feldspar dissolution in mol (feldspar) L^{-1} s^{-1}; $r'_+ = r_+ \cdot S_A$
r_-	Reverse rate of feldspar dissolution reaction (precipitation or formation) in mol (ab) m^{-2} s^{-1}; similarly, for r'_-
r_{2nd}	Precipitation rate of secondary mineral in mol (Si) m^{-2} s^{-1}; similarly, for r'_{2nd}
r'_{pre}	$r'_{pre} = vr'_- + r'_{2nd}$, defined as "precipitation rate" in mol L^{-1} s^{-1}
$r'_{pre,Si}$	The total Si-containing phase precipitation rate measured in Si (mol Si L^{-1} s^{-1})
$r'_{pre,Al}$	The total Al-containing phase precipitation rate measured in Al (mol Al L^{-1} s^{-1})
S_A	Surface area load of feldspar (m^2/L) in the reactor; $S_A = s_A$*m/V, where m denotes the mass (g) of reactant, V the volume of solution in the reactor, and s_A the specific surface area (m^2/g). e.g., 0.143 m^2/g*1.0 g/0.01L for albite
T	Temperature (K)
t	Time (s)
Δt	Time interval from time t to time t + 1
V	The volume of the solution in a reactor (L)
[X]	The total concentration of element or species X
$[X]^t$	The total concentration of element or species X at time t
v_{ab}	The stoichiometric coefficient in the molecular formula of albite
v_{pre}	The stoichiometric coefficient of the secondary precipitation phase
Abbreviations*	
ab	Albite
am	Amorphous
aq	Aqueous species
kln	Kaolinite
pre	Precipitation
SI	Saturation index

*Mineral abbreviations follow Siivola and Schmid (2007).

ate their relationship with $\Delta_r G$. In contrast, isotope tracer methods generate a different kind of dissolution rates: unidirectional dissolution rates, r_+ (Gruber et al., 2013, 2014; Liu et al., 2016; Zhu et al., 2016; Gong et al., 2019; Zhu et al., 2020). While r_{net} is a function of $\Delta_r G$,

$$r_{net} = r_+ - r_- = k_+ f(\Delta_r G) \quad (3)$$

r_+ and k_+ are independent of $\Delta_r G$ but depend on reaction mechanisms. If reaction mechanisms do not change when an experimental solution approaches near-equilibrium conditions, we should see a constant k_+ across $\Delta_r G$, regardless of whether there is secondary phase precipitation (Fig. 1). If reaction mechanisms switch from a mechanism operating in the far-from-equilibrium region to another in the near-equilibrium region, we should see k_+ change as a two-step function of $\Delta_r G$ (Fig. 1). The test of many hypotheses of reaction mechanism near-equilibrium becomes much more straightforward with r_+ than r_{net} data.

2.1. Hypothesis 1: two mechanisms across a critical $\Delta_r G$

Several near-equilibrium experiments have shown that the r_{net} vs $\Delta_r G$ relationship has a sigmoidal shape (Burch et al., 1993; Taylor et al., 2000; Hellmann and Tisserand, 2006). Burch et al. (1993) used the empirical rate equation below to describe the relationship:

$$r_{net} = k_{+,1}\left(1 - \left(e^{n\Delta_r GRT}\right)^{m_1}\right) + k_{+,2}\left(1 - \left(e^{\Delta_r GRT}\right)\right)^{m_2} \quad (4)$$

where $k_{+,1}$ and $k_{+,2}$ denote the rate constants in units of mol m^{-2} $s^{-1,}$ and n, m_1, and m_2 are empirical parameters fitted from experimental data (Zhu, 2009). Eq. (4) suggests two parallel mechanisms that dominate under far-from-equilibrium and near-equilibrium conditions, respectively (Burch et al., 1993; Beig and Lüttge, 2006; Hellmann and Tisserand, 2006; Lüttge, 2006) (We will use the term "parallel rate law" after Maher et al. (2009) hereafter in this communication). At far-from-equilibrium conditions, specifically when $\Delta_r G > \Delta G_{crit}$ (ΔG_{crit} is a critical free energy level above which the screw dislocation etch pits will not open up), the dissolution mechanism involves etch-pit opening, which is faster and dominates the dissolution process. At near-equilibrium conditions, etch pit opening is prohibited, and step retreat is the only dissolution mechanism. Thus, the dissolution rate is significantly slower. The formulation of Eq. (4) results in two rate plateaus in different ranges of $\Delta_r G$ (cf. Fig. 1).

Burch et al. (1993) and Hellmann and Tisserand (2006), using the concentration-based method available at that time

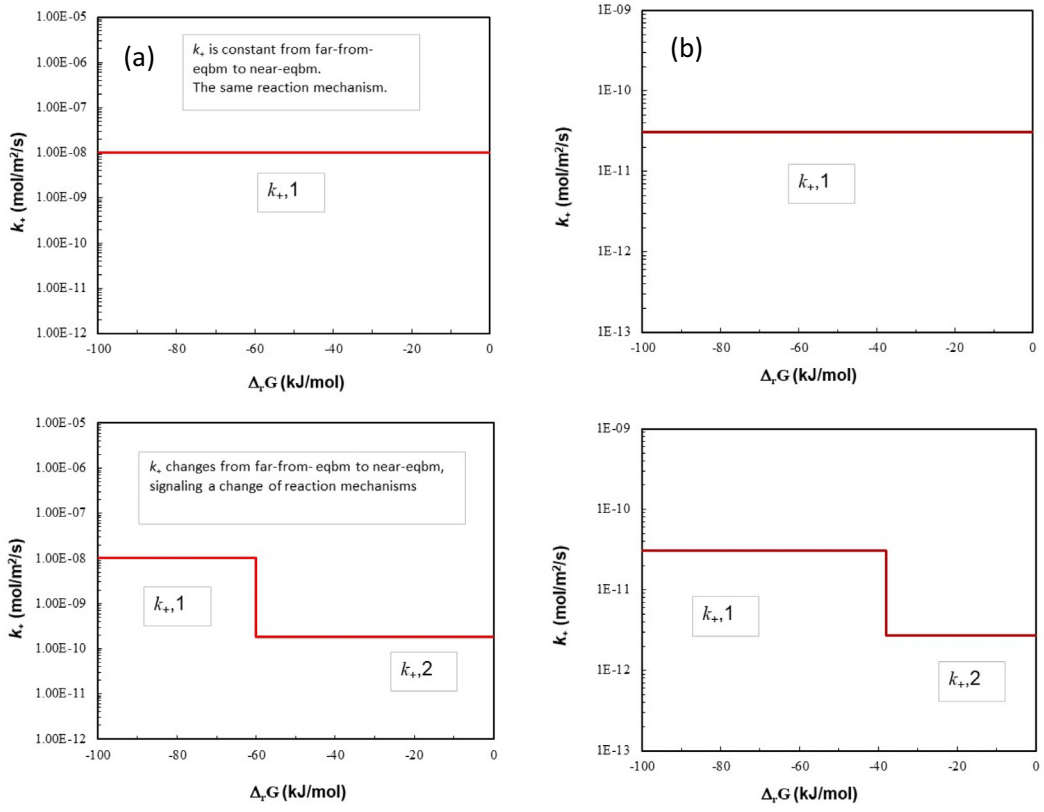

Fig. 1. Relationship between "intrinsic" rate constants and Gibbs free energy of reaction ($\Delta_r G$) for one-step mechanism and two-step mechanisms. The left panel resembles the albite dissolution experiment conditions of Hellmann and Tisserand (2006) at 150 °C and pH 9.2. The right panel resembles the albite dissolution experiment conditions of Burch et al. (1993) at 80 °C and pH 8.8. Note that the critical $\Delta_r G$ of mechanism switch and step reduction are different ($k_{+,1}$ is 11.16 times larger $k_{+,2}$ in Burch et al. (1993) and 56.67 times larger in Hellmann and Tisserand (2006).

(Hellmann and Tisserand (2006) also used albite weight loss), measured net reaction rates. From these data, they retrieved k_+ values. The "intrinsic" rate constant k_+, is a residual property after subtracting the $\Delta_r G$ effects. If a small amount of Si precipitation occurred, that was embedded into the rate constants too. In this study, we measured r_+ directly. Assuming no significant changes in S_A, we obtained k_+ values from r_+ values across a range of $\Delta_r G$. This constitutes a more direct test of the change mechanism hypothesis.

2.2. Hypothesis 2: Secondary phase precipitation

Another possibility for the observed lower dissolution rates near equilibrium is the artifact of secondary phase precipitation as it is asserted by some authors (e.g., Alekseyev et al., 2004). In the near-equilibrium region, the [Al] and [Si] are high, and the experimental solutions are supersaturated with several amorphous and crystalline secondary phases. The precipitation of a Si-containing secondary phase will lower the apparent dissolution rates and produce artifacts of the reduced rates.

The change in Si concentration in unit time would be better termed the *apparent net reaction rate*. The apparent net reaction rate ($\tilde{r}_{net}$) of albite is the combination of rates of albite dissolution, albite precipitation, and Si-containing secondary precipitation (Eq. (5))

$$\tilde{r}_{net} = \frac{d[Si]}{dt} = vr_+ - vr_- - r_{2nd} \quad (5)$$

Therefore, previous studies of albite dissolution kinetics in the literature all measured $\tilde{r}_{net}$, which includes the reverse reaction and secondary phase precipitation. Some authors have carefully examined possible secondary phase precipitates using SEM, XRD, and TEM and presented convincing evidence of stoichiometric Si:Al release that indicated no significant amount of secondary precipitation (Burch et al., 1993; Berger et al., 2002; Hellmann and Tisserand, 2006). The concern for potential secondary phase precipitation in near-equilibrium experiments restricted previous studies to highly alkaline or acidic pH (Table 2). However, Si isotope tracers are much more sensitive than XRD or Si:Al ratios for detecting the precipitation of a Si-containing phase, and Si isotope tracer methods have shown that secondary phase precipitation is more commonplace than previously realized (Zhu et al., 2016, 2020).

2.3. Hypothesis 3: Al inhibition

Several studies have suggested that Al ions inhibit the dissolution of many aluminosilicate minerals, such as albite (Chou and Wollast, 1985; Oelkers et al., 1994), K-feldspar (Gautier et al., 1994), kaolinite (Devidal et al., 1997), kyanite (Oelkers and Schott, 1999), basalt glasses (Oelkers and Gislason, 2001), and muscovite (Oelkers et al., 2008). In the near-equilibrium region where Al concentration is high, the role of $\Delta_r G$ is also significant (Blum and Stillings, 1995; Lasaga, 1998). Unidirectional rates can provide testing of this hypothesis, in addition to isotach graphs. For example, Schott et al. (2009, their Eq. (35)) gave this rate equation:

$$r_{net} = k_+ \left[\frac{K * \left(\frac{a_{H^+}}{a_{Al^{3+}}^{1/3}} \right)}{1 + K * \left(\frac{a_{H^+}}{a_{Al^{3+}}^{1/3}} \right)} \right] (1 - \exp(\Delta_r G / 3RT)) \quad (6a)$$

where K^* denotes a Langmuir sorption constant for the activated surface precursor. The r_+ data would separate the two effects and would help test this hypothesis in the near-equilibrium region.

$$r_+ = k_+ \left[\frac{K * \left(\frac{a_{H^+}}{a_{Al^{3+}}^{1/3}} \right)}{1 + K * \left(\frac{a_{H^+}}{a_{Al^{3+}}^{1/3}} \right)} \right] \quad (6b)$$

2.4. Hypothesis 4: Na inhibition

Stillings and Brantley (1995) showed that albite dissolution rates at pH 3 were slower by about an order of magnitude in a 0.1 M NaCl solution. However, Gruber et al. (2019) found that albite dissolution only slightly decreased from 10^{-5} to 10^{-2} m NaCl solutions, but about three times faster in 1 m NaCl solution than the rate in the control solution of 10^{-5} m NaCl. Their experiments were conducted at pH 5, 25 °C, and far-from-equilibrium conditions. Theoretically, if H_3O^+-Na^+ exchange is an important part of the albite dissolution mechanism, the Na:H ratio in solution should affect albite dissolution rates. However, different levels of Na^+ concentration also mean different levels of $\Delta_r G$. The concentration-based method obtains r_{net}, which would be a function of both [Na^+] and $\Delta_r G$, making a test of the Na^+ inhibition hypothesis difficult at near-equilibrium conditions. The r_+ values are independent of $\Delta_r G$ but can be measured at different levels of

Table 2
Experimental conditions in albite near-equilibrium albite experiments.

Authors	T °C	pH	$\Delta_r G$ kJ/mol min	max	$\Delta_r G$ /RT min	max	$\Delta_r G_{crit}$
Burch et al. (1993)	80	8.8	−46	−2	−15.7	−0.7	−38
Hellmann and Tisserand (2006)	150	9.2	−150	−15	−42.6	−4.2	−58
Alekseyev et al. (1997)	300	9	−75	−14	−15.8	−2.9	
Oelkers et al. (1994)	150	9	−56	−6	−16.0	−1.6	n/a
Beig and Luttge (2006)	185	9	−61	−10	−16.0	−2.7	−61
Alekseyev et al. (2004)	300	9	−42	0	−8.8	0	
This study	50	8	−26	−2	−10.1	−0.7	

[Na^+]. These data can be used to test this hypothesis more effectively at near-equilibrium conditions.

3. MATERIALS AND METHODS

3.1. Albite grains preparation

Albite mineral samples (from Bancroft, Ontario, Canada) were purchased from the WARD'S Natural Sciences Establishments, Inc. The crystals were crushed with a jaw crusher and disc pulverizer, then ground with a shatter box and subsequently sieved through a clean copper mesh to retain the size fraction between 53–106 μm. In the freshly ground material, many submicron-to-micron-sized particles adhered to the surface of large grains. The dissolution of these ultra-fine particles results in initially non-linear rates of reaction or parabolic kinetics (Holdren and Berner, 1979). To remove these particles, the ground feldspar sample was ultrasonically rinsed with ethanol eight times for about 20 minutes per treatment. After cleaning, the treated sample was dried in an oven at 60 °C overnight.

The cleaned samples were then pretreated to reduce the high-energy sites on the surface. ~ 1 kg of cleaned samples were added to a 1L HDPE bottle. ~ 500 mL DI water was then added to the bottle until it was almost full, and all solids were fully submerged. The bottles were then put in a water bath at 50 °C for 4 weeks. The water was changed every week. After pre-treatment, the water was decanted, and the crystals were rinsed with ethanol three times to remove the residue water. The rinsed particles were dried in an oven at 60 °C overnight and ready for use.

Powder X-ray diffraction (XRD) analyses were performed using a Rigaku Rapid II diffraction system (Mo Kα radiation, $\lambda = 0.70930$ Å) with 50 kV and a 100-μm diameter collimator. Powder albite sample was packed into a 1.1 mm outer diameter, 1.0 mm inner diameter polyimide tube. During measurement, polyimide tube was rotating in Phi direction to randomize crystal orientations. Signals were collected using a 2-D image-plate detector. Raw patterns were integrated using Rigaku 2DP software. Mineral phase identification was determined using the MID Jade 9.5 software package with coupled American Mineralogist Crystal Database (AMCSD) and the PDF-4 + database from the International Centre for Diffraction Data (ICDD). The analysis showed peaks of ordered albite and no detectable amounts of other minerals.

A Beckman Coulter SA-3100 surface area analyzer was used for the BET (Braunauer et al., 1938) surface area analysis of albite grains before the experiments. The samples were degassed at 250 °C overnight prior to measurements. The instrument was calibrated before and periodically during measurements, using the National Institute of Standards and Technology reference material 1900, a silicon nitride powder with a surface area of 2.85 m^2/g. Multipoint N_2 gas adsorption isotherms were measured to obtain BET-specific surface area of samples (Lu et al., 2013). The specific surface area of albite was 0.143 m^2/g with an analytical error within ± 10%.

Scanning Electron Microscopy (SEM) was conducted with a Quanta 400 Field Emission Gun (FEG). The Energy Dispersive X-ray Spectrometer (EDS) system has an EDAX thin window and CDU LEAP detector. The low energy X-ray detection with FEG provided high spatial resolution for microanalysis down to ~ 0.1 μm^2 under optimum conditions.

3.2. Batch experiment set-up

The experiment solution was prepared by mixing ^{29}Si stock solution (prepared following the same procedures as in Zhu et al., 2020), $Al(NO_3)_3 \cdot 9H_2O$, $NaNO_3$ solid, and DI water. pH was adjusted with 1 N HNO_3 and 1 N NaOH solution to pH = 5 ± 0.2. 20 ml of the solution was taken as blank samples. A portion of the blank samples was acidified by adding 2–3 drops of concentrated HNO_3 per 10 ml of solution. Different levels of departure from equilibrium with respect to albite were achieved by varying the Na, Al, and Si concentrations. See Table 3 for the experimental matrix.

Thereafter, various amount (see Table 3) of the mineral sample (53–106 μm), and 15 g stock solution (equivalent to 15 mL) was mixed in a wide-mouth polypropylene bottle

Table 3
The experiment matrix.[a]

Experiment #	pH	Na (μM)	Al (μM)	Si (μM)	Solid:Solution
Ab1	5	0	0	0	4.5 g:15 ml
Ab2	5	0	0	2	4.5 g:15 ml
Ab3	5	50	1	10	4.5 g:15 ml
Ab4	5	50	1	20	4.5 g:15 ml
Ab5	5	50	1	50	4.5 g:15 ml
Ab6	5	50	1	100	4.5 g:15 ml
Ab7	5	100	1	200	10 g:15 ml
Ab8	5	100	3	200	10 g:15 ml
Ab9	5	100	3	300	15 g:15 ml
Ab10	5	100	3	500	30 g:15 ml
Ab11	5	500	3	500	30 g:15 ml
Ab12	5	500	5	600	30 g:15 ml
Ab13	5	1000	10	600	30 g:15 ml

[a] The actual concentrations in solutions slightly deviated from the design slightly. See Tables in EA samples with time zero notation.

(30 ml size) to initiate mineral dissolution. Overall, eight polypropylene bottles were prepared for the group of batch experiments, including 2 duplicates. They were sealed with Parafilm, put in a water bath at 50 °C, and manually agitated and mixed twice a day.

3.3. Sampling of dissolution experiments

Samples were collected at 1hr, 5hr, 10hr, 24hr, and 48hr. Two replicate samples are taken at the first and fifth sampling events for quality control. When collecting samples, the solution in the bottle was poured into a syringe installed with a 0.22 μm filter to separate the solids from the solution. The filtrate was then separated into three portions for pH measurement and Si concentration analysis, cation analysis, and silicon isotope analysis. The solids left in the bottle were thereafter rinsed with several mL ethanol five times to wash off the residual solution, transferred into a plastic container with a spoon, air-dried overnight, and then stored. In order to make the solution unsaturated with respect to potential secondary phases (e.g., kaolinite, gibbsite, imogolite, allophane, amorphous SiO_2 and $Al(OH)_3$), the solution for cation analysis was acidified with 1 to 2 drops of 12 N HCl solution.

3.4. Sample analysis

Total dissolved Si concentrations (i.e., [Si]) were analyzed with Perkin Elmer Lambda 2S UV–visible spectrophotometer, using the molybdate blue method (Govett, 1961). The uncertainty in measured Si was less than ± 5% for concentrations above 4 μM. Detection limits for analyses of Si were less than 0.5 μM. Total concentrations of Na^+, Al^{3+}, and K^+ were analyzed with inductively coupled plasma–quadrupole mass spectrometry (ICP-QMS) Agilent 7700x with a measurement uncertainty of ± 5%. The detection limit for analyses of Al was about 10 ppb.

The Si isotope ratios and composition analyses were performed with a Nu Plasma 1700 (Nu Instruments, UK) high-resolution multiple-collector inductively coupled plasma mass spectrometry (HR-MC-ICP-MS) system installed in the State Key Laboratory of Continental Dynamics, Northwest University, Xi'an, China. Silicon isotope analyses on MC-ICP-MS require high-mass resolving capabilities to resolve polyatomic species that interfere with the Si mass-spectrum, the three silicon isotopes were subjected to the following interferences: ($^{14}N_2^+$, $^{12}C^{16}O^+$) for $^{28}Si^+$, ($^{14}N_2^1H^+$, $^{12}C^1H^{16}O^+$, $^{15}N^{14}N^+$) for $^{29}Si^+$, and ($^{14}N^{16}O^+$) for $^{30}Si^+$. These interfering peaks cannot be effectively separated in conventional low-resolution mode (<1000 RP, resolving power) and are at the high-mass side of the Si isotopes (Georg et al., 2006; Yuan et al., 2016). The Nu Plasma 1700 can provide resolving power sufficient to resolve all polyatomic species that interfere with the Si mass-spectrum. Isotope analyses are typically performed in high resolution with a resolving power of $m/\Delta m = 10000$. During mass-spectrometric analyses, all three Si isotope masses were measured simultaneously to overcome intrinsic noise associated with the plasma ion-source to ensure that isotope ratios are determined with good precision. Standard and samples (~0.5 μg/g Si) were introduced into the plasma via a self-aspirating microconcentric PFA nebulizer. Silicon backgrounds were corrected for by on-peak-zero measurements, where a blank solution (2% HNO3) was analyzed instead of a sample. The blank intensities (normally < 0.05 V) were then subtracted from the signals of the subsequent sample analyses. Typical signal intensities for an uptake rate of 0.1 ml/min were approximately 10 V for a solution containing 1 μg/g Si. Instrumental mass discrimination was corrected by using the standard-sample bracketing (SSB) technique, and the typical precision better than 0.1‰ (2SD).

3.5. Retrieval of reactions from isotope tracer data

Dissolution rates (r_+) were best-fitted by solving the mass balance equations for Si and Si isotopes. These equations and their behaviors in the batch reactor systems were described in detail in Zhu et al. (2016, 2020). Here we present the equations and terminology again for the flow of discussion. In a batch reactor system, we have the following mass balance equations:

$$\begin{cases} [\mathrm{Si}]^{t+1} = (\nu r'_{+} - r'_{pre})\Delta t + [\mathrm{Si}]^{t} \\ [\ ^{28}\mathrm{Si}]^{t+1} = (\nu f_{28,ab} r'_{+} - f_{28,t} r'_{pre})\Delta t + f_{28,t}([Si]^{t^0} + (\nu r'_{+} - r'_{pre})\sum_{t=t^0}^{t}\Delta t[\mathrm{Si}]^{t}) \\ [\ ^{29}\mathrm{Si}]^{t+1} = (\nu f_{29,ab} r'_{+} - f_{29,t} r'_{pre})\Delta t + f_{29,t}([Si]^{t^0} + (\nu r'_{+} - r'_{pre})\sum_{t=t^0}^{t}\Delta t[\mathrm{Si}]^{t}) \end{cases} \quad (7)$$

The only unknowns are the dissolution rate r'_+ and precipitation rate of the Si-containing phase r'_{pre}. For convenience, we call the scenario without Si precipitation (set r'_{pre} as zero) Model A. We call the scenario with Si-containing phase precipitation Model B ($r'_{\mathrm{pre}} > 0$).

3.6. Speciation and solubility modeling

Based on the measured concentrations of Si, Al, Na, and pH, saturation indices (SI) for albite and aluminosilicate minerals were calculated with the aid of the software PHREEQC 3.6.4 (Parkhurst and Appelo, 2013). An internally consistent dataset of equilibrium constants for relevant mineral and aqueous species at 50 °C was constructed using SUPCRTBL (Zimmer et al., 2016). Equilibrium constants (log K) for selected reactions can be found in the Electronic Annex.

Because the level of departure from equilibrium is the key aspect of this study, we repeat here the sources of thermodynamic properties for speciation-solubility modeling. Standard state thermodynamic properties for mineral endmembers were taken from Holland and Powell (2011) unless otherwise noted. For allophane and imogolite, the thermodynamic properties were re-calculated based on Su and Harsh (1994; 1998) and Stefansson (2001) to ensure the thermodynamic properties were internally consistent with the rest of the SUPCRTBL database (Zimmer et al., 2016). The thermodynamic properties for Al-bearing aqueous species were taken from Tagirov and Schott (2001); SiO_2^0(aq) from Miron et al. (2016), which was based on Rimstidt (1997); and rest of the aqueous species from Shock and Helgeson (1988), Shock et al. (1989), Shock et al. (1997), and Sverjensky et al. (1997). The T and P

dependences of thermodynamic properties for aqueous species, when applicable, were predicted using the parameters of the revised HKF equations of state for aqueous species (Helgeson et al., 1981; Tanger and Helgeson, 1988). For amorphous SiO_2 and $Al(OH)_3$, the log *K*s were taken from Stefansson and Gislason (2001). Activity coefficients for the charged aqueous species were calculated from the B-dot equation fitted to mean salt NaCl activity coefficients (Oelkers and Helgeson, 1990). Activity coefficients for neutral or uncharged aqueous species were calculated from the Setchénow equation with a coefficient of 0.1 (PHREEQC).

In evaluating the aqueous speciation and mineral saturation states at experimental conditions, we used the pH and total analytical concentrations of the constituents measured at ambient conditions (i.e. ~22 °C and 1 bar) as input into the modeling program and then "re-heated" the solution to experimental *T* and *P*. This method calculates the *in situ* pH at the experimental conditions by taking account of the effects of *T* and *P* on the distribution of aqueous species (Zhu and Lu, 2009).

4. EXPERIMENTAL RESULTS

All experimental analyses are provided in the Electronic Annex as well as at Indiana University's institutional data repository IUScholarWorks, which can be accessed via this link at http://hdl.handle.net/2022/25805.

4.1. Silicon isotope fractions, Si concentrations, and albite dissolution rates

The ^{28}Si, ^{29}Si, and ^{30}Si isotope fractions (f_{28}, f_{29}, f_{30}) in the experimental solutions changed significantly during the experiments (Fig. 2), providing ample resolution for the retrieval of dissolution rates, r_+. The ^{30}Si isotope fractions (f_{30}) were much smaller and their values are less precise. Therefore, the discussion below is based on f_{28} and f_{29} data. As found in previous studies, there is a short period of "hiatus" or "excursion" after albite grains were first put into contact with the solution. This was manifested in a sharp rise of f_{28} and a decrease of f_{29} within the first hour. The increase of f_{28} and a decrease of f_{29} with time were noticeably fast between 1 and 10 hrs. The isotope composition changes slowed with time and became almost linear between 10 and 48 hours. Our analysis below focuses on the steady-state dissolution reactions between 10 and 48 hours. As described in Section 3, the albite grains were pre-treated in dilution solutions for four weeks before the experiments.

The temporal evolutions of [Si] varied, depending on the level of initial [Si] in the starting solutions (Fig. 3). For experiments initiated at low [Si], [Si] increased throughout the experiment (i.e., Ab2). For experiments starting with 10–100 μM (Ab3-Ab6), [Si] increased from 1 hour to 10 hours, and then [Si] slightly decreased over time. For experiments that started with 200–600 μM Si (Ab6-Ab13), [Si] decreased over time (Fig. 3, left panel).

Because we knew total Si concentrations and the fractions of Si isotopes in the experimental solutions, the concentrations of the individual Si isotopes could be calculated. Precipitation of a Si-containing phase(s) during the experiments was demonstrated by the decrease of [^{29}Si] over time (Fig. 3, right panel). Our initial solutions contained almost pure ^{29}Si. Isotope exchange occurred, particularly when the albite grains first came in contact with the solutions (see data in EA). However, isotope exchange (defined as isotope changes without net change of total Si) after 10 h was unlikely to take up that much ^{29}Si from the solutions (e.g., >100 μM/L for Ab-12). In short, two lines of evidence indicate Si-containing phase precipitation: a) the predicted [Si] values from dissolution rates were much higher than actual measured [Si] values (Fig. 3 left column); and b) [^{29}Si] values decreased in Ab3-Ab13.

To retrieve r_+ and $r'_{pre,Si}$, the mass balance equations for Si and ^{29}Si described in Section 3.5 (Model B) were solved simultaneously with the aid of the Excel® solver. A weight factor of 500 was applied to f_{29} over [Si]. Rates for two time-segments of 1–10 hours and 10–48 hours were retrieved. The rates discussed hereafter are for 10–48 hours (steady state). One albite unidirectional dissolution rate fitted f_{28}, f_{29}, and f_{30} data simultaneously (Fig. 2). The r_+ values for Ab2-Ab13 are tabulated in Table 4. Experiment Ab1 was not spiked with ^{29}Si in order to start very far-from-equilibrium. The Si concentration data were scattered and did not produce a dissolution rate.

The precipitation of a Si-containing phase affected the isotope fractions in the experimental solutions negligibly when only a small amount of Si was precipitated. This is indicated by the overlap of the lines of Model A and Model B in Fig. 2 for Experiment Ab2-Ab9. However, in experiments with high Si concentrations (Ab10-Ab13), Model B must be used to fit both isotope data and Si concentration data simultaneously in order to retrieve the dissolution rates. No values of r_+ alone can satisfactorily fit the Si isotope data.

It is clear from Fig. 3 that a significant amount of Si was precipitated in experiments that were near equilibrium. The amount of precipitated Si can be calculated from the albite dissolution rate and mass balance. For Ab13, the initial solution has 435 μM Si. 290 μM Si was released to the solution from albite dissolution. A total of 586 μM Si was precipitated. The Si concentration as well as f_{28}, f_{29}, and f_{30} temporal evolution resulted from the combined albite dissolution and precipitation of a Si-containing phase. However, the mass balance equations have taken into account these sources and sinks. A single rate r_+ fit all three isotopes consistently (Fig. 2). Since the mass balance equations Eq. (7) did not contain fractionation terms, this confirms that isotope fractionation was negligible in our experimental systems in terms of reaction rate determination.

It is also clear from Fig. 3 that in these near-equilibrium experimental systems, Si concentrations failed to provide true albite dissolution rates. In all experiments, precipitation of a Si-containing phase occurred. In some experiments (Ab6-Ab13), net decreases of [Si] were observed. To obtain near-equilibrium conditions, Si concentrations in the initial solutions were high. Attempts to reach near-equilibrium by an increase of Al concentrations in the initial solution were not successful because Al quickly precipitated out. Efforts to start with solutions with a stoichiometry of Si:Al:Na of 3:1:1 were also unsuccessful.

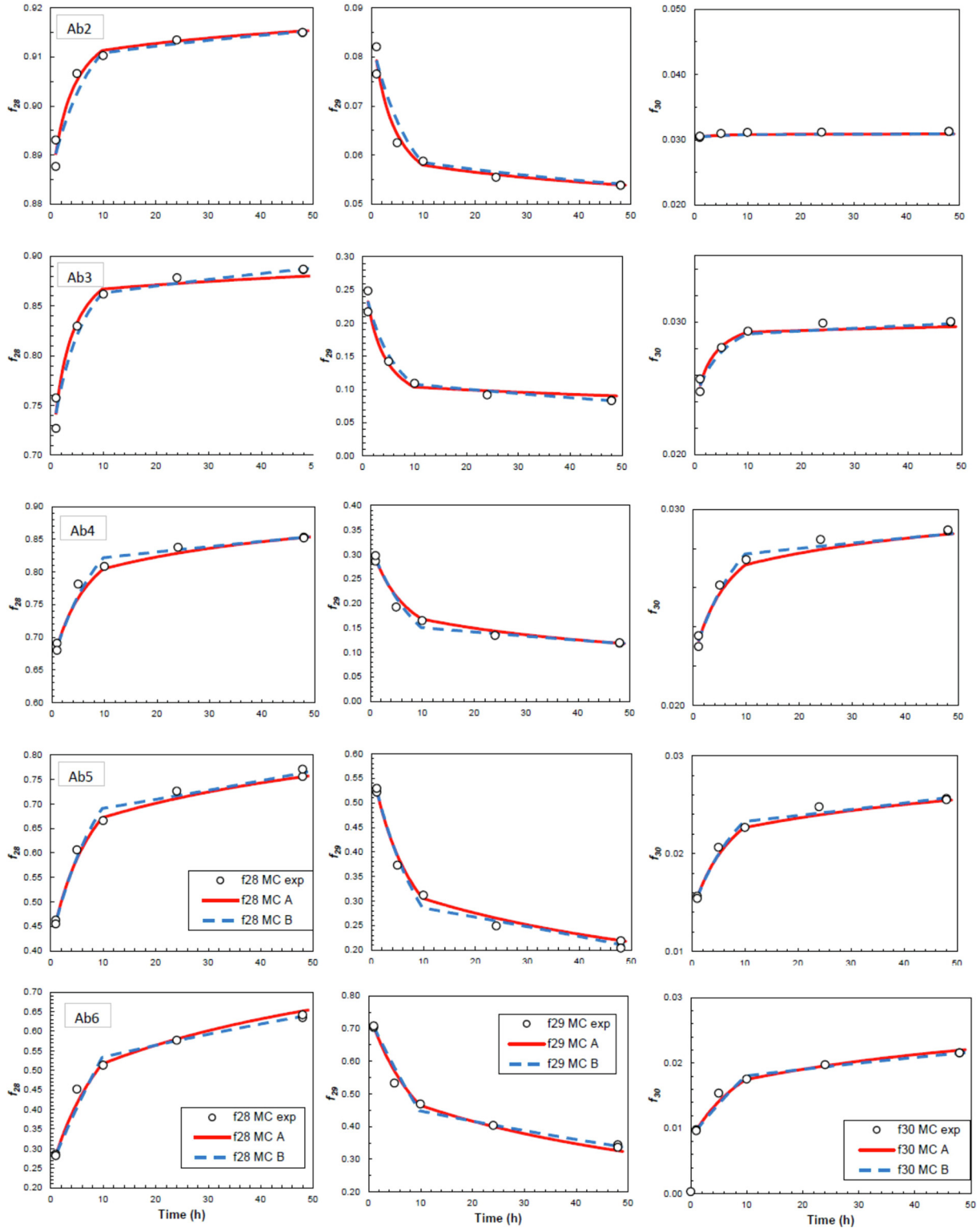

Fig. 2. Temporal evolution of Si isotope fractions in experimental solutions. Symbols represent experimental data. Analytical uncertainties for isotope fraction (f_{28} and f_{29}) are less than $\pm$ 0.001(2σ), which is smaller than the symbols. Red and blue lines were calculated from Eq. (7) assuming without (Model A) and with (Model B) Si precipitation, respectively.

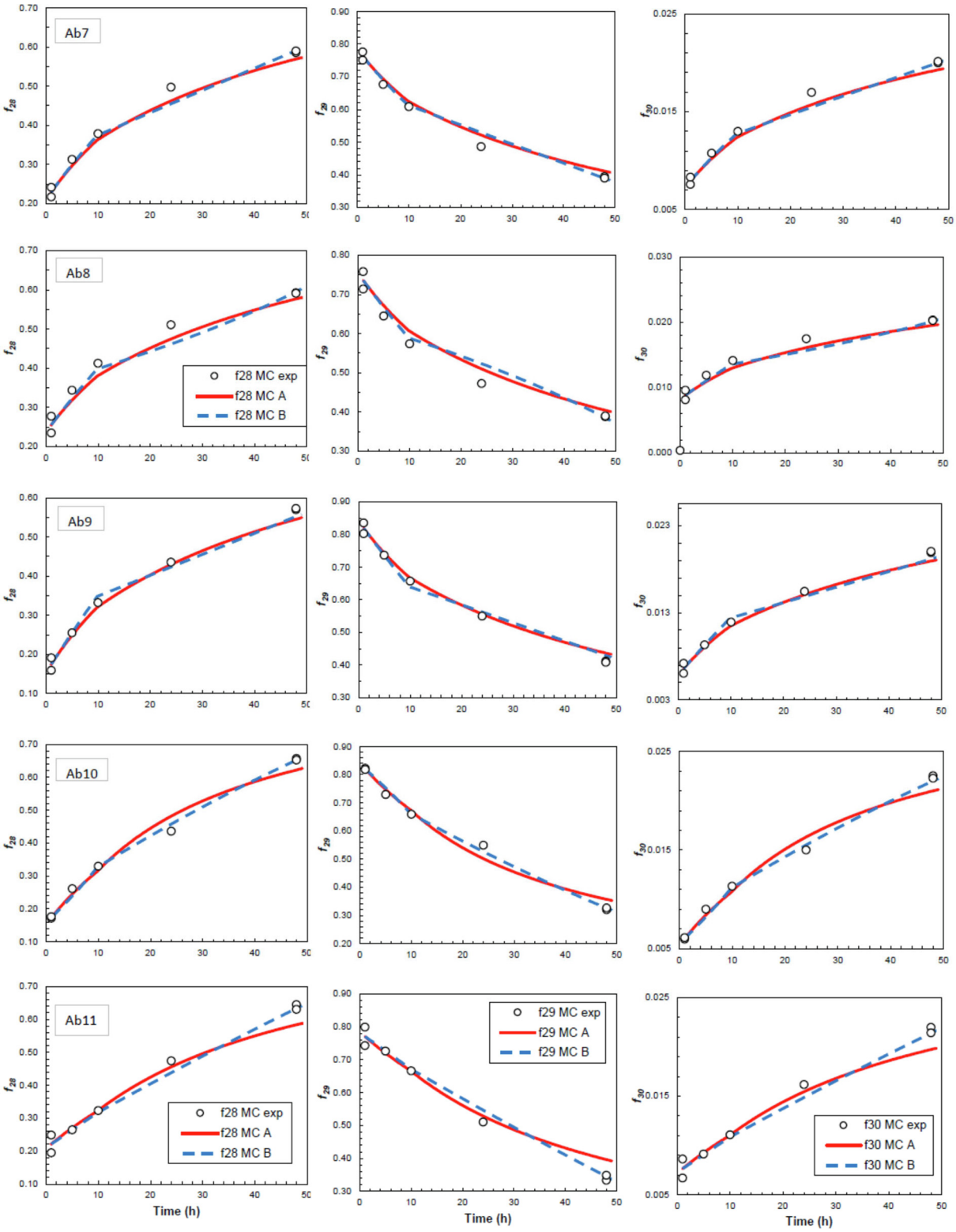

Fig 2. *(continued)*

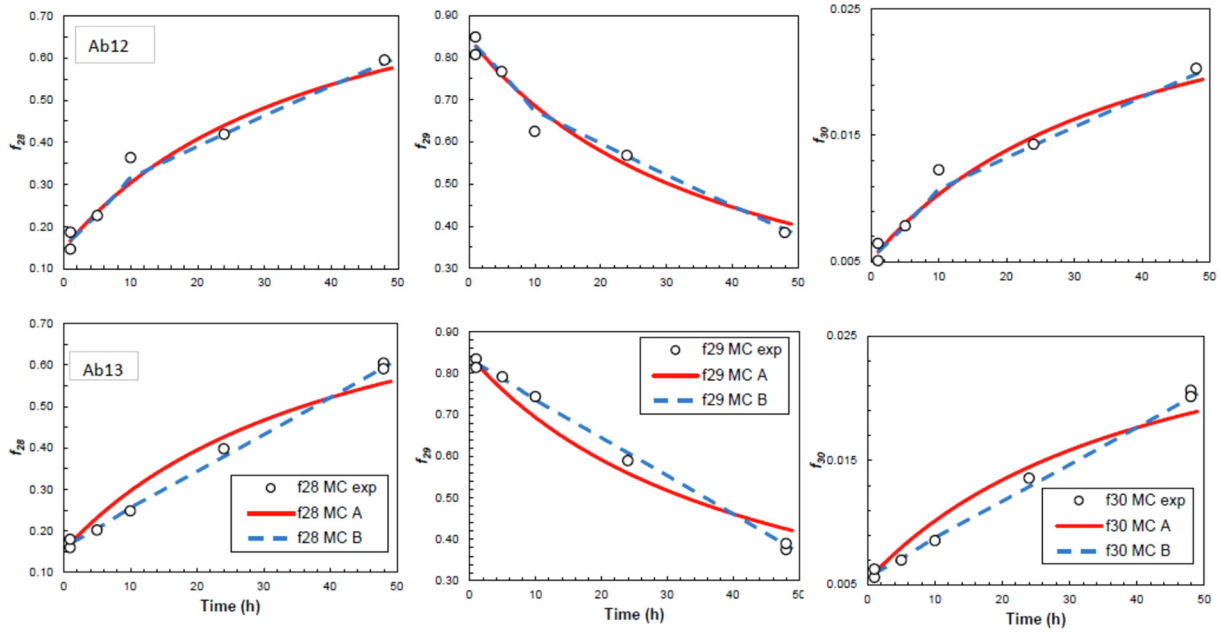

Fig 2. *(continued)*

However, isotope data cannot tell us which Si-containing secondary phase was precipitated. Both SEM and TEM characterization of the precipitate were unsuccessful. The bulk rates of Si-containing phase precipitation (mol Si L^{-1} s^{-1}) are listed in Table 4.

4.2. pH and Al and Na Concentrations

The pH measured at 22 °C varied within a band between 8.5 to 8.75 (See the Electronic Annex). The calculated in situ pH at 50 °C were narrowly distributed around 8 and varied between 7.75 and 8.25. The pH values were almost constant in the batch series.

Measured Al concentrations for fluids passing the 0.2 μm filter are listed in the Electronic Annex. [Al] increased with reaction time, but samples at 48 hours in three lower saturation experiments had [Al] drop significantly. These samples also had lower measured pH at ambient temperature. It is not clear whether it was due to the precipitation of an Al-bearing secondary phase during sample handling or analysis. However, the higher saturation experiments yielded consistent [Al] values. As discussed below, all these concentrations appear to be artificially too high.

After a sharp increase immediately after the contact between the initial solution and albite grains, the Na concentrations increased approximately linearly in all 13-experiment series (See the Electronic Annex).

4.3. Mineral saturation indices

The calculations of quartz and amorphous SiO_2 saturation indices were not affected by the Al analysis issues discussed below. All experimental solutions were undersaturated with amorphous SiO_2. Some samples in very near equilibrium experiments were supersaturated with quartz (Fig. 4).

It is well-known that Al concentrations in near-neutral solutions are difficult to determine. White (1995) used both Al analytical values and calculated [Al] values assuming that soil waters are at equilibrium with amorphous Al $(OH)_3$. We followed this practice and calculated two sets of saturation indices (SI) for aluminosilicates in this study. At 50 °C, the likely precipitating Al hydroxide phase is gibbsite. Below, we will first present SI values assuming the solutions were saturated with gibbsite.

For batch experiment series with lower starting Si, Al, and Na concentrations (Ab1 to Ab6), albite saturation indices slightly increased during the experimental duration (Fig. 5). For batch experiments with higher starting concentrations (Ab10 to Ab13), the saturation indices for albite decreased over time, corresponding to a decrease of [Si]. Overall, the experiments covered a large range of albite saturation. In terms of $\Delta_r G/RT$, the range was −10.1 to −0.7. In terms of $\Delta_r G$, the values ranged from −25.86 to −1.88 kJ/mol or a span of 24 kJ/mol.

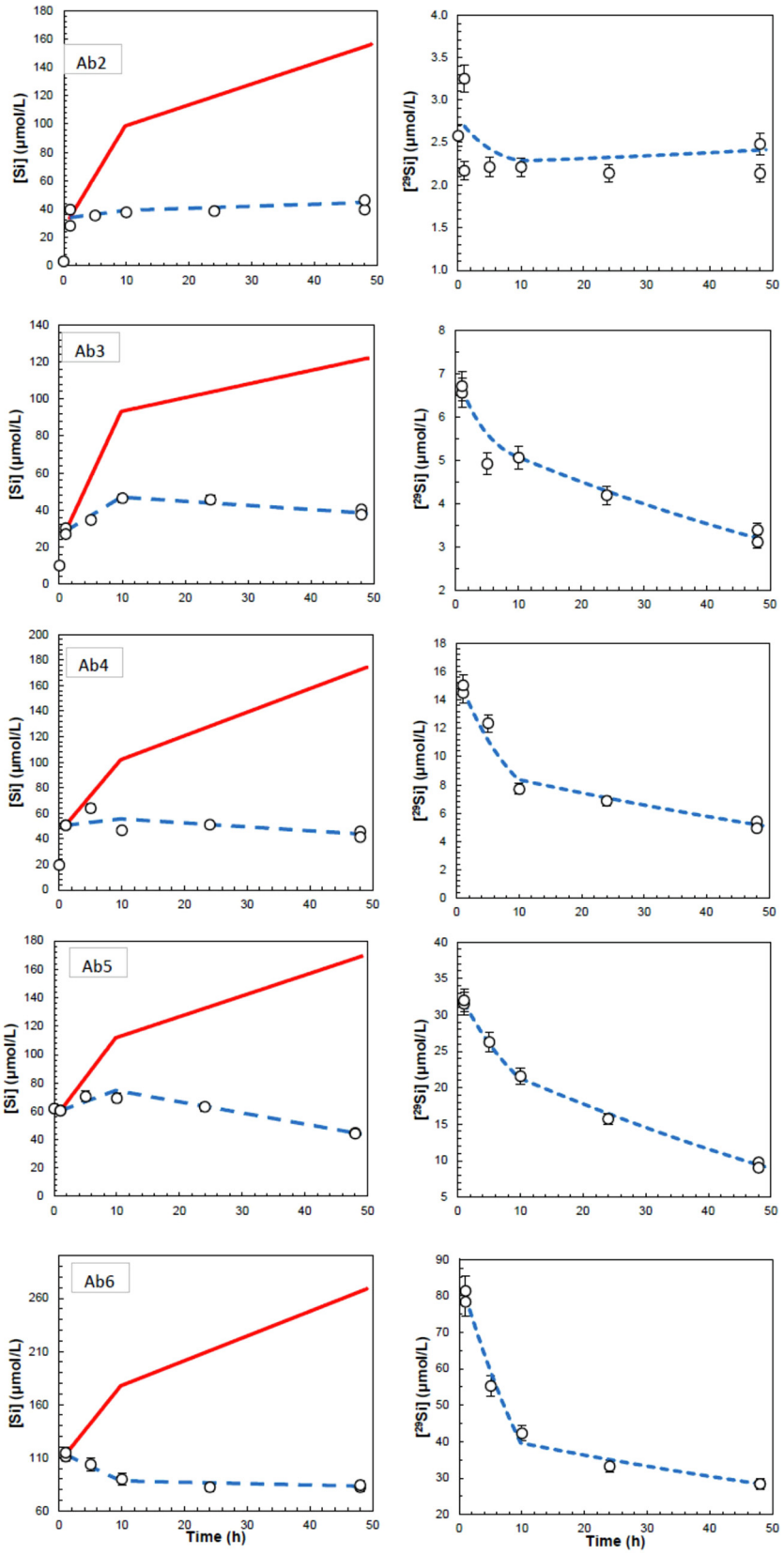

Fig. 3. Temporal evolution of total Si concentrations [Si] in experimental solutions. Symbols represent experimental data. Error bars on [^{29}Si] data used ± 5% (2σ) analytical uncertainties for Si. The uncertainties for isotope fraction (f_{28} and f_{29}) are less than ± 0.001(2σ). Red and blue lines were calculated from mass balance equations assuming without (Model A) and with (Model B) Si precipitation, respectively.

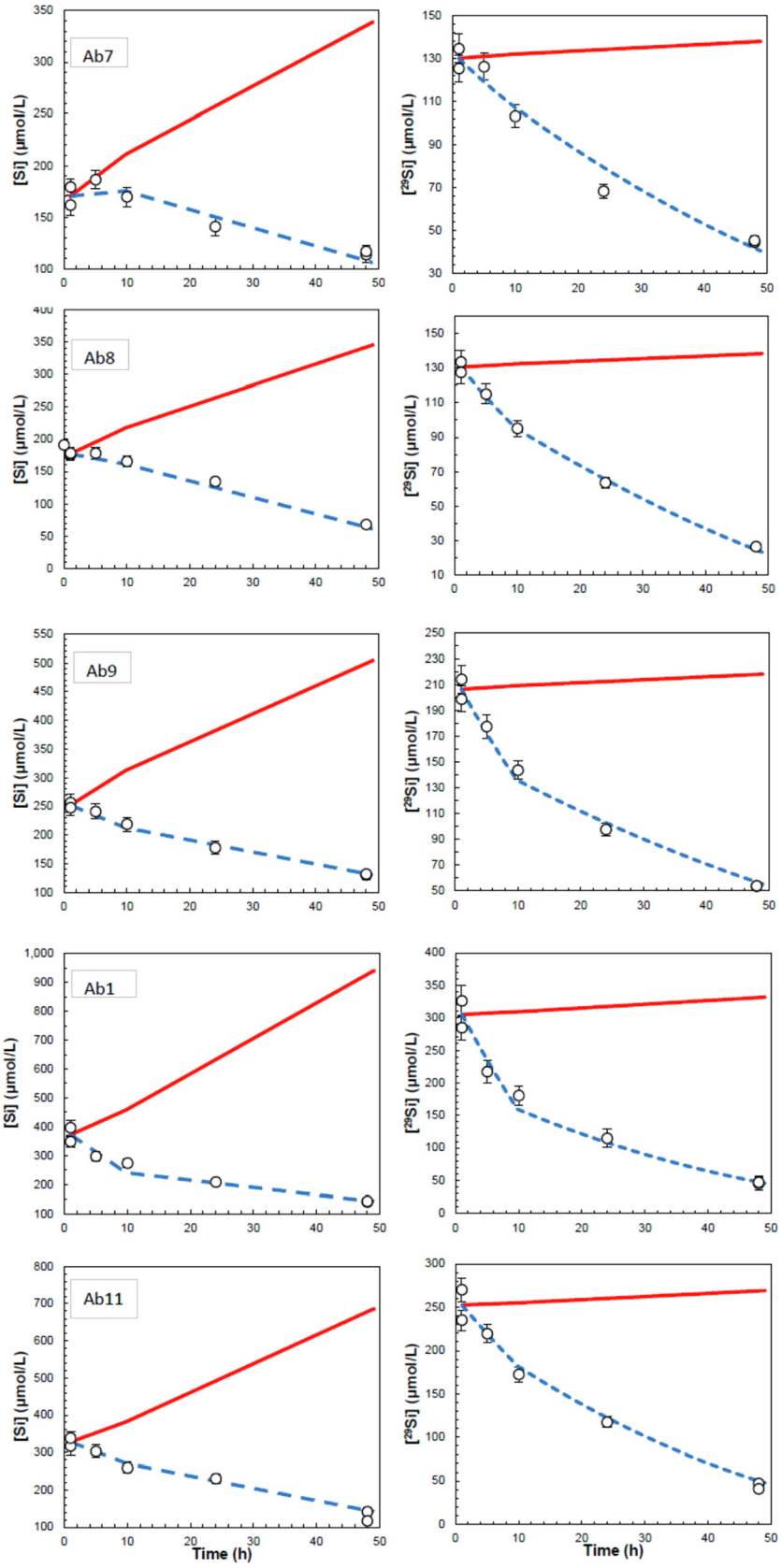

Fig 3. *(continued)*

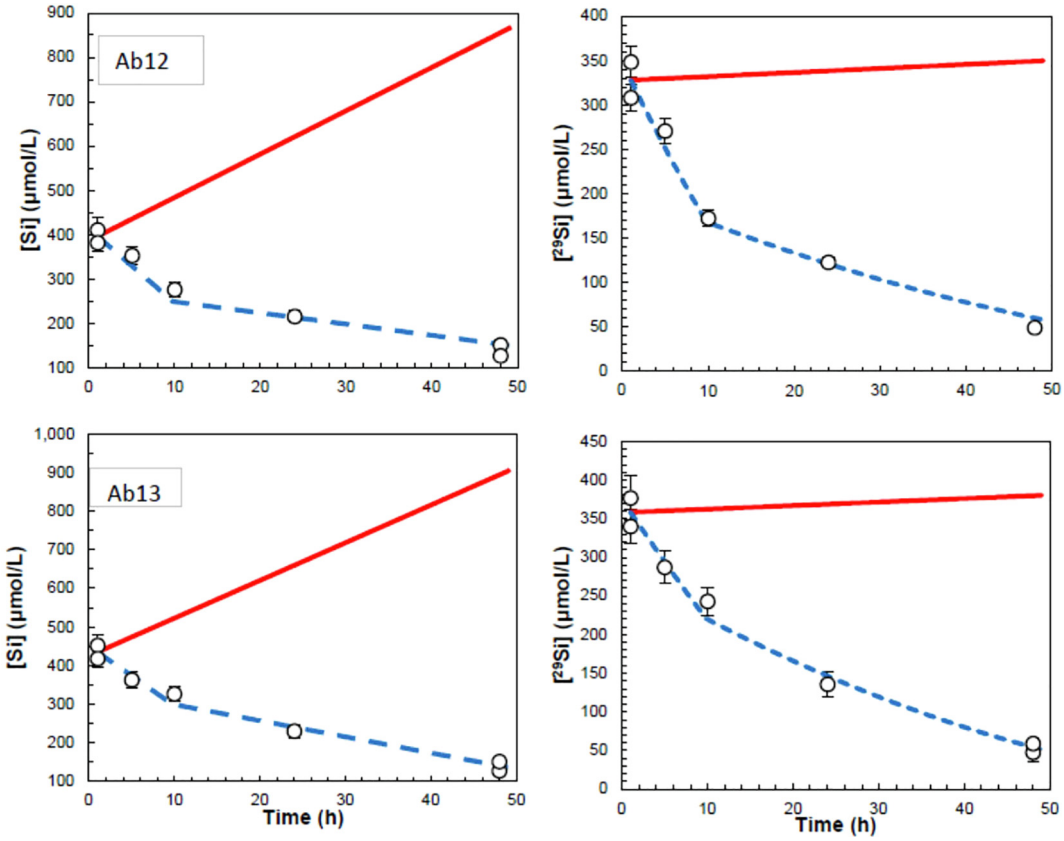

Fig 3. *(continued)*

Table 4
Steady-state dissolution and Si precipitation rates fitted from Model B.

Expt ID	log $r+$ (mol ab m^{-2} s^{-1})	log r'_{pre} (mol Si L^{-1} s^{-1})	$\Delta_r G/RT$ at $t = 24$ h
Ab2	−11.96	−9.99	−3.0
Ab3	−11.90	−9.65	−3.7
Ab4	−11.98	−9.66	−3.2
Ab5	−11.91	−9.42	−2.8
Ab6	−11.82	−9.64	−2.4
Ab7	−11.75	−9.00	−1.8
Ab8	−11.90	−8.97	0.1
Ab9	−11.90	−8.95	0.0
Ab10	−11.90	−8.75	0.9
Ab11	−11.90	−8.70	1.5
Ab12	−12.0	−8.81	2.0
Ab13	−11.90	−8.65	1.5

All experimental solutions were supersaturated with respect to kaolinite. Experimental solutions of higher series were supersaturated with respect to imogolites and allophanes (Fig. 6), and numerous other aluminosilicates.

We also used the analytical [Al] data for calculating saturation indices for aluminosilicates for comparison. The speciation-solubility calculations showed albite supersaturation in some experiments. This will be discussed in the next section.

5. DISCUSSION

5.1. Comparison with rate data in the literature

The unidirectional albite dissolution rates (r_+) obtained in this study are comparable to r_+ values in Zhang (2019) who conducted similar Si isotope tracer dissolution experiments for albite at pH 5.2 to 6.4 (Fig. 7). The unidirectional rates can be compared to far-from-equilibrium rates

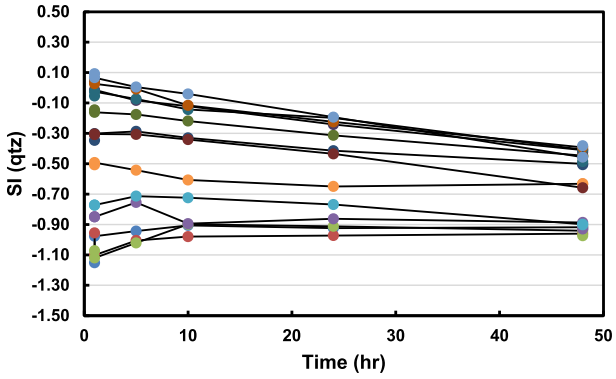

Fig. 4. Temporal evolution of saturation indices (SI) of quartz. Symbols represent experimental data, and lines connect experimental data of the same experiment series. For duplicate samples, the averages are plotted.

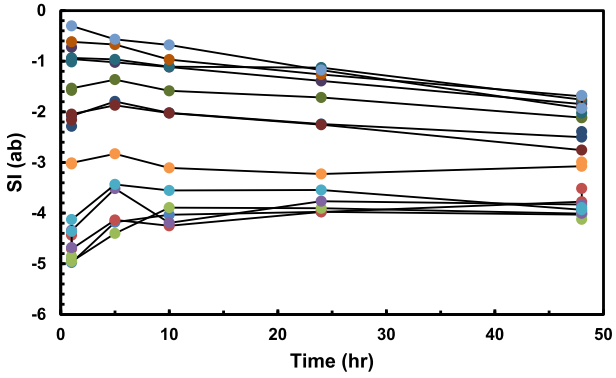

Fig. 5. Temporal evolution of saturation indices (SI) of albite. Symbols represent experimental data, and lines connect experimental data of the same experiment series. SI values were calculated with Al concentrations calculated from equilibrium with gibbsite.

reported in the literature a) if far-from-equilibrium reaction mechanisms are identical to near-equilibrium ones, and b) if experimental conditions are the same (e.g., pH, $[Al^{3+}]$, $[Na^{+}]$, ionic strength, experimental duration, sample preparation).

The far-from-equilibrium rate in the literature that was measured under experimental conditions closest to this study was from Gruber et al. (2016). Using the concentration-based method based on [Si], Gruber et al. (2016) measured an albite dissolution rate of 6.14×10^{-12} mol s^{-1} m^{-2} at 50 °C, pH ~ 5, and $\Delta_r G \sim$ -100 kJ/mol. Their rate was calculated from three [Si] data points sampled before 9 hours of reaction. This rate is 4.5 times faster than the rates based on isotope tracers by Zhang (2019) at pH 5.2 and rates in this study at pH ~ 8 (Fig. 7). Gruber et al. (2016) did not use any of their late-stage data (from 9 to 726 h) for rate calculation because after 9 hours, the Si:Al ratios became greater than the albite stoichiometry, and [Si] no longer increased linearly with time. Thus, they suspected the precipitation of an Al-and Si-containing phase. The meticulous experiments of Gruber et al. (2016)

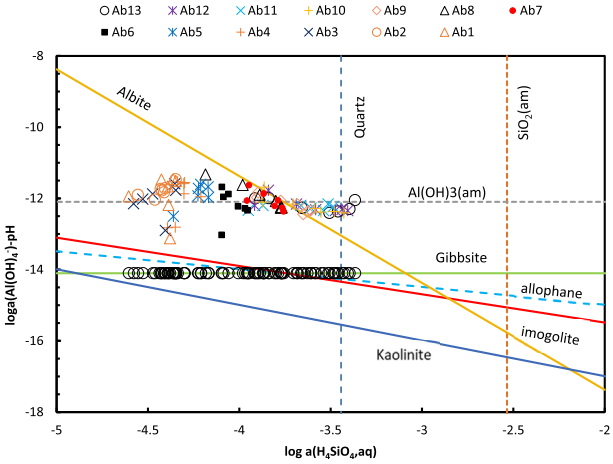

Fig. 6. Saturation state of solution samples with respect to selected minerals in the system Al_2O_3-SiO_2-H_2O. The solubility boundaries were calculated at 50 °C and 1 bar using thermodynamic properties listed in Zhu et al. (2020). The albite line was calculated by using the median log a_{Na+} value of −3.27. Color symbols represent experimental data with [Al] concentrations of solution passing 0.22 μm filters. Experiments Ab1 to Ab13 progressed toward equilibrium with respect to albite. The black circles represent calculations assuming Al was controlled by equilibrium with gibbsite.

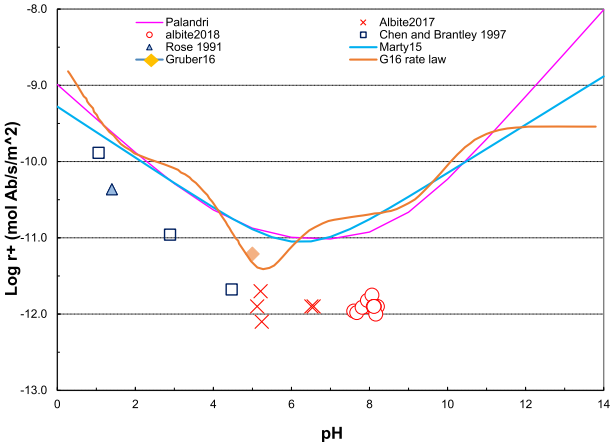

Fig. 7. Dissolution rates r_+ are plotted as a function of pH. Rates of "albite2017″ (Zhang, 2018; Zhu et al. 2020) and "albite2018" (this study) are near-equilibrium unidirectional dissolution rates from Si isotopes. Rates from the literature are far-from-equilibrium dissolution rates. Palandri and Marty15 denote the rate constant compilation of Palandri and Karkare (2004) and Marty et al. (2015), respectively. "G16 rate law" stands for the proposed surface complexation model of Gruber et al. (2016). Note that the data show that albite dissolution is independent of pH in the range of 5–8 (Chen and Brantley, 1997; Rose, 1991).

underscore the challenges of using the concentration-based method to measure feldspar dissolution rates even under far-from-equilibrium conditions ($\Delta_r G \sim -100$ kJ/mol). It can be extrapolated that experiments closer to equilibrium ($\Delta_r G > -100$ kJ/mol) are more likely to precipitate secondary phases. The isotope tracer method pioneered by

Gruber et al. (2013) should be the method of choice for near-equilibrium experiments.

Fig. 7 also shows that our rates are about one order of magnitude slower than the recommended values for far-from-equilibrium rate for albite by Palandri and Kharaka (2004) and Marty et al. (2015). These kinetic rate compilations provided empirical rate laws regressed from rates at a wide range of temperature and pH.

5.2. A switch of reaction mechanisms at a critical $\Delta_r G$?

Fig. 8 shows that the dissolution reaction rates r_+ did not vary as a function of the distances from equilibrium in our experiments. As illustrated in Fig. 1, a switch of reaction mechanisms would show two rate plateaus. Therefore, it appears that one dominant reaction mechanism operates within a range of $\Delta_r G \sim 24$ kJ/mol in this study. If the one data point of Gruber et al. (2016), described in detail in Section 5.1, is used, then there is no mechanism-switch from $\Delta_r G$ of −100 to −2 kJ/mol at 50 °C. The idea of mechanism-switch was based on previous experiments in strongly alkaline pH solutions (see Table 2). No experimental data in the circum-neutral pH region were available (Gruber et al. (2014) did not cover a wide range of $\Delta_r G$). It is possible that the etch pit opening mechanism does not operate under near-neutral pH conditions.

A thorough and comprehensive review of the screw dislocation, hollow core, and etch pit opening mechanism at far-from-equilibrium was given by Luttge et al. (2019). In the literature, the critical energy, $\Delta_r G_{crit}$, for which etch pit opening will not occur when $\Delta_r G > \Delta_r G_{crit}$, has been evaluated from the surface energetic and mineral crystallographic views. However, chemical reaction mechanisms may not be independent of the etch pit mechanisms. For example, previous experiments were conducted at alkaline conditions under which the OH-catalyzed mechanism was dominant (see Table 2). In contrast, experiments in this study were conducted in near-neutral pH conditions under which an H_2O-catalyzed mechanism is dominant (see below in Section 5.3). The energy barrier for etch pit opening for the H_2O-catalyzed mechanism is probably higher. Etch pit opening may not be as pervasive or significant in near-neutral pH as in alkaline or acidic conditions. Notably, we conducted experiments at a lower temperature than those in Table 2.

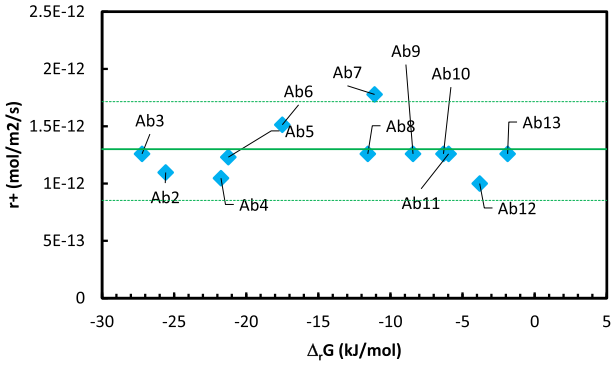

Fig. 8. Albite unidirectional dissolution rates as a function of departure from equilibrium ($\Delta_r G = 0$). The diamonds denote experimental rates from this study. The labels (e.g., Ab-2) indicate experiment ID. The solid line signals the mean and dashed lines bound the two standard deviations from the mean. $\Delta_r G$ values were calculated from speciation-solubility modeling using the thermodynamic properties for albite from Holland and Powell (2011), Al-species from Tagoriv and Schott (2001), and SiO_2^0(aq) species based on Rimstidt (1997), and equilibrium with gibbsite. The use of thermodynamic properties recommended by Miron et al. (2016) would shift the symbols to left by −0.89 and those recommended by Tutolo et al. (2014) by −0.2.

Another possible explanation is that the etch pit opening mechanism exists, but our experiments had already passed the $\Delta_r G_{crit}$ point and were on the second rate-plateau (Figs. 1 and 9a). The far-from-equilibrium rates are orders of magnitude higher than the one data point from Gruber et al. (2016).

A third alternative explanation is that the mineral surface history played a dominant role Luttge et al. (2019). Because all albite grains came from the same batch with the same preparation, the density of etch pits was the same in experiments at far-from-equilibrium (Gruber et al., 2016) and near-equilibrium (this study). The short reaction time and low temperature did not reset the mineral surface history. However, this explanation is highly speculative. Detailed etch pit data are not available in this study or in Gruber et al. (2016).

Davis et al. (2011) found a switch of mechanism occurred very close to equilibrium with quartz (∼−0.8 kJ/mol), which they attributed to a switch from Q^2 site dissolution to Q^1 site dissolution in addition to the mechanism switch at much further away from equilibrium (Q^3 site to Q^2 site). We did not observe a second mechanism switch for albite in our study.

Clearly, additional experimental data are critical. Much of the debate in the literature relied on re-interpretations of a few experimental data points obtained decades ago. Future studies should attempt to cover far-from-equilibrium to near-equilibrium regions (e.g., $\Delta_r G \sim 0$ to <-60 kJ/mol), vary the duration, pH, reactor-types, and temperatures, and characterize secondary phases with a variety of techniques. It would likely be fruitful to combine solution chemistry and isotopes with VSI characterization of mineral surface morphology. Most of the near-equilibrium experiments have been performed on albite. Experiments on other silicate minerals are needed. By all means, near-equilibrium experiments are a challenge. Only repeated experiments that generate a critical mass of experimental data can test this hypothesis effectively.

5.3. Testing other hypotheses of near-equilibrium reaction mechanisms

While it is well known that feldspar dissolution is strongly pH-dependent (Blum and Stillings, 1995), there is a controversy about whether there is an H_2O-catalyzed reaction mechanism in near-neutral pH in addition to the H^+- and OH^--catalyzed reaction mechanisms in acidic and basic pH solutions, respectively. See Gruber et al. (2016) for a thorough review. This issue is significant for

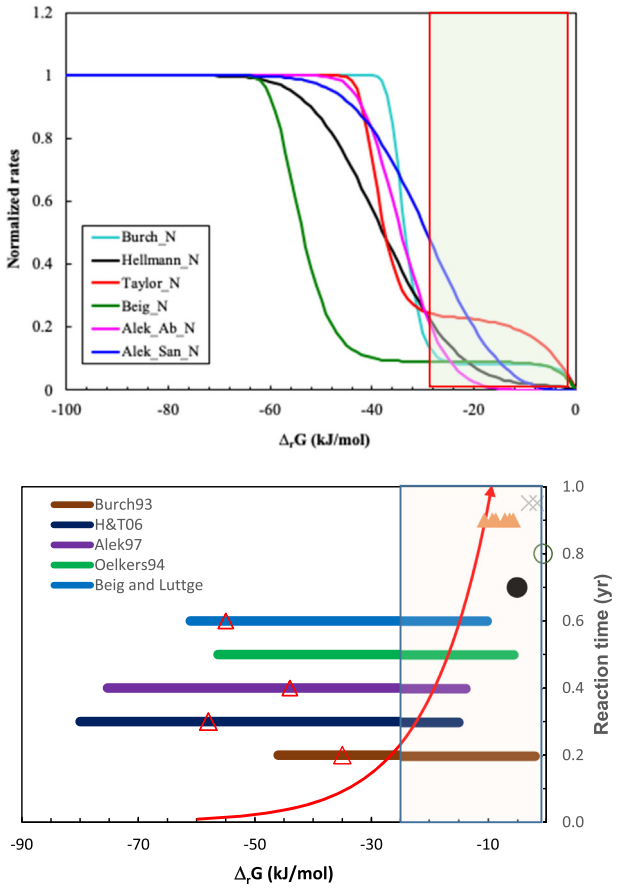

Fig. 9. (a) Parallel rate laws that model two mechanisms: one rate plateau for far-from-equilibrium and another near-equilibrium, proposed by various authors as noted. (b) The range of $\Delta_r G$ covered in previous experiments and this study (shaded area). The triangles denote the $\Delta_r G_{crit}$ values where the mechanism switch was supposed to happen. The shaded box of ~ 25 kJ/mol is the range of albite saturation in this study. The RHS y-axis shows the time after reacting with albite, which shows that an almost pure aqueous solution only needs to react with albite for a short time to pass the critical $\Delta_r G$ values greater than $-40 \sim -60$ kJ/mol region. The saturation states of natural water are also plotted on the graph. The black circle and open circle: median surface water groundwater from Langmuir (1997), respectively. Orange triangles: groundwater in the Navajo sandstone at Black Mesa, Arizona, USA (Georg et al., 2009). Grey crosses: weathering profiles at Santa Cruz, California (Maher et al., 2009).

two reasons. First, as discussed in Section 5.2, a question arises whether the hypothesis of etch pit opening mechanism derived from OH^--catalyzed dissolution under alkaline conditions can be extrapolated to H_2O-catalyzed dissolution under circum neutral pH conditions. Second, as a practical matter, what overall rate law should be used in reactive transport models for modeling natural systems mostly under circum neutral pH conditions.

Part of the controversy arises from the paucity of near-neutral pH rate data or the reliability of these data in the circum-neutral pH range. Al- and Si-containing secondary phase tend to precipitate under neutral pH conditions, which make near-neutral pH rate data particularly suspect. Gruber et al. (2016) pointed out "it is impossible to conclude unequivocally from the existing data sets that water-promoted mechanism does not exist due to the high analytical noise of the experimental data and the low resolution of the data as a function of pH."

Traditionally, the three reaction mechanisms of H^+, H_2O, and OH^- catalysis are represented by a separate rate constant $k_{neutral}$ and apparent activation energy Ea for the water-catalyzed mechanism (Hellmann, 1994; Blum and Stillings, 1995):

$$r_+ = k_{25}^{H} a_{H^+}^{nH} exp[\tfrac{-E_a^H}{R}(\tfrac{1}{T} - \tfrac{1}{298.15})] + k_{25}^{neutral} exp[\tfrac{-E_a^{neutral}}{R}(\tfrac{1}{T} - \tfrac{1}{298.15})] + k_{25}^{OH} a_{H^+}^{nOH} exp[\tfrac{-E_a^{OH}}{R}(\tfrac{1}{T} - \tfrac{1}{298.15})] \quad (8)$$

where nOH is negative to use a_{H+} to account for the OH^- catalysis. The widely used rate – pH curves from kinetics data compilations (Palandri and Kharaka, 2004; Marty et al., 2015) are shown in Fig. 7. The formulation of Eq. (8) has been widely used in geochemical models. However, as Gruber et al. (2016) pointed out, these models are empirical and are based on the bulk solution a_H^+ rather than feldspar surface chemistry.

Other authors recognize only H^+- and OH^--promoted reaction mechanisms (Schweda, 1990). Recently, Gruber et al. (2016) proposed a surface complexation model-based pH-dependent rate law (Wieland et al., 1986; Blum and Lasaga, 1991; Stumm, 1992). They assumed two surface sites on albite and regressed the surface complexation constants from literature data. Their rate law predicted a minimum at about pH 5 (Fig. 7).

Here, this study provides new data of r_+ in the circum-neutral pH range. Our rates confirm that within pH 5–8, albite dissolution is independent of pH (Fig. 7), which is consistent with rate – pH patterns at far-from-equilibrium found in the literature (Chou and Wollast, 1984; Knauss and Wolery, 1986; Hellmann, 1994). These rates using the Si- and Al-concentrations are prone to artifacts of secondary phase precipitation in the near-neutral pH range (see Section 5.1 and the quote of Gruber et al. (2016) on data quality). We can argue that rates from isotope tracers are more reliable than those by the concentration-based method, given the challenges described in Gruber et al. (2016) with secondary phase precipitation even at far-from-equilibrium. Our new r_+ data support either the presence of an H_2O-promoted catalysis mechanism or call for a revision of the Gruber et al. (2016) rate law. The Gruber et al. (2016) approach has a clear advantage in that it is based on feldspar surface coordination chemistry. More experimental data in the near-neutral pH range are needed.

In general, the experimental datasets on the pH-dependence of silicate mineral dissolution rates are spotty (Palandri and Kharaka, 2004; Brantley, 2008). Most experimental data are at acidic pH. Rather than refitting scant experimental data points from old experiments in the literature, again and again, new experimental data in the near-neutral and alkaline pH should be obtained to build a more complete database of pH-dependence, which will allow us to decipher reaction mechanisms less ambiguously. The Si isotope tracer method facilitates such a new effort.

To achieve different levels of departure from equilibrium with respect to albite, the activities of Na^+ in our experiments varied from 1.8×10^{-3} to 1.8×10^{-4} M. The question arises whether Na inhibition or enhancement of albite dissolution was a factor in our experiments, which would compromise the objective of isolating the $\Delta_r G$ effects in the experiments. However, r_+ values did not vary noticeably with a_{Na^+} in this range. This is consistent with the finding of Gruber et al. (2019).

However, high Na^+ concentration solutions likely have high Si and Al concentrations as well, which makes it necessary to de-convolute the $\Delta_r G$ and Na effects. The longest duration in the seawater experiment of Gruber et al. (2019) had a $\Delta_r G$ of ~ -16 kJ/mol, which is in the near-equilibrium region according to Gruber et al. (2014). Future work should extend to 1 m NaCl solution in the experiment matrix presented in Table 3 while keeping Al and Si concentrations high enough to be relevant to natural waters.

The Al concentrations in the initial solutions also varied in this study to achieve different levels of departure from equilibrium with respect to albite (Table 3). The Al inhibition hypothesis calls for rate variation with $\log(a_{H^+}/a_{Al^{3+}}^{1/3})$ (see Eq. (6b)) or equivalently $\log a_{Al(OH)_4^-} - pH$. Our near-equilibrium experiments Ab7-Ab13 had nearly constant $\log a_{Al(OH)_4^-} - pH$ values for a range of $\Delta_r G$ (Fig. 6), which indicates that our r_+ values were de-convoluted from the effects of [Al]. However, as shown in the following section, the Al concentration data are suspect, which keeps us from having a meaningful discussion about the Al inhibition effects. Future research will focus on a wider range of [Al] in experiments and use different types of reactors.

5.4. Uncertainties in experimental data and interpretations

The largest uncertainty of this study is whether Al colloids passed the 0.22 μm filters in our samples. All the discussions of rate variation with respect to distance from albite equilibrium were based on the assumption that they did, and that the dissolved Al concentrations were controlled by equilibrium with gibbsite. Calculated dissolved [Al] was two orders of magnitude lower than the analytical values (Fig. 6). Using either analytical [Al] or calculated [Al] (equilibrium with amorphous $Al(OH)_3$) result in supersaturation of albite. As shown in Fig. 6, the [Al] concentrations in the very near-equilibrium experiments (Ab7-Ab13) fell on the $Al(OH)_3$(am) solubility line. In short, the lack of reliable Al concentrations weakens all arguments of $\Delta_r G - r_+$ relationship put forward in this communication.

Of lesser concern are the uncertainties of $\Delta_f G^o$ for albite and aqueous species. As long as we used the same $\Delta_f G^o$ value for albite for all samples, the calculated range of $\Delta_r G$ is reliable. For example, using the $\Delta_f G^o$ value for albite recommended by Tutolo et al. (2014) would shift the calculated $\Delta_r G$ by −0.5 kJ/mol in Fig. 8. It is also interesting that the albite saturation indices calculated using the thermodynamic properties compiled in SUPCTTBL and from the llnl.dat database have an average difference of 0.14 ± 0.02 (2 SD). The llnl.dat database uses the $\Delta_f G^o$ value for albite from Helgeson et al. (1978), Al species and SiO_2^0(aq) species in Johnson et al. (1992).

The other uncertainty is the apparent parabolic behavior of Na in some low saturation series experiments, which could be due to the batch reactor artifacts (Oelkers et al., 2001). Future studies will include reaction path modeling to take into account the Al inhibition effects and the changing concentrations of other constituents.

5.5. Implications for geochemical modeling

To quantitatively evaluate environmental and geological processes such as geological carbon sequestration, nuclear waste disposal, diagenesis, and weathering, results from geochemical kinetic studies such as this study must be incorporated into macroscopic geochemical models. Our experiments were in the near-equilibrium region at Si, Al, Na concentrations, and pH resembling the majority of natural surface and ground water (Langmuir, 1997). Langmuir (1997) reported a median value of 274 and 1305 μM for Na, 233 and 266 μM for Si, 0.37 and 0.37 μM for Al for surface and ground water, respectively. The first implication from these experiments is that, in the circum-neutral pH region, where most natural waters are, a term for the H_2O-catalyzed reaction mechanism should be included in rate laws. From the discussions earlier, the parallel rate law with a mechanism-switch is probably not applicable in the pH range of 5–8.

The parallel rate law is also not significant from the point of view of saturation states. The switch of etch pit mechanisms reported in the literature (see Table 2) occurs at a critical $\Delta_r G$ of −40 to −60 kJ/mol away from albite equilibrium. This is in solutions much more dilute than the surface and ground water range cited above, e.g., 10 times more dilute than Langmuir's median river water. The $\Delta_r G$ for albite in the median surface water reported in Langmuir (1994, Table 8.8) is −5.14 kJ/mol (−0.9SI) and in the median groundwater it is −0.6 kJ/mol (SI of −0.11). Soil water reported by White (1995) is also more concentrated. The soil water from the Santa Cruz soil chronosequence, California, USA has $\Delta_r G$ of −3.1 to −1.7 kJ/mol (Maher et al., 2009). Fig. 9b compares these $\Delta_r G$ ranges. Therefore, the etch pit opening hypothesis, codified by the parallel rate law (Burch et al., 1993), may not be critical for modeling natural waters.

If one looks at this issue from a temporal point of view, only a short period of time is required for almost pure water to react with albite and reach closer to equilibrium than the −40 to −60 kJ/mol region. Fig. 10 shows the results of reaction path modeling. It would take < 0.05 years for the solution to evolve from almost pure water to have a $\Delta_r G >$ -40 kJ/mol using the one-mechanism TST rate law of Marty et al. (2015). Using the same rate constant but two-mechanisms $f(\Delta_r G)$ function in Eq (4), it would also take < 0.05 years for the solution to evolve from almost pure water to $\Delta_r G > -40$ kJ/mol. In other words, the rates only stayed on $k_{+,1}$ rate plateau for < 0.1 years (Fig. 10b). Geochemical modeling simulation in support of geological carbon sequestration concerns time periods of > 10,000 years and nuclear waste disposal 10^4–10^6 years

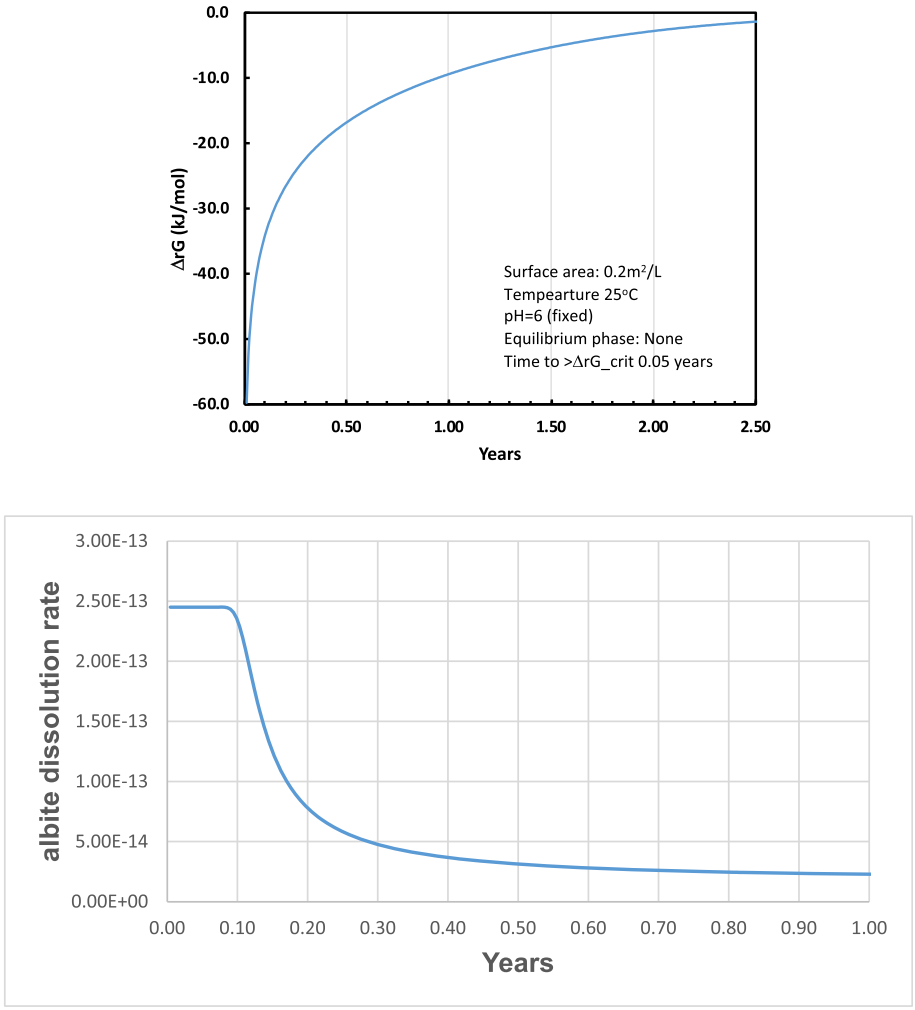

Fig. 10. Results of reaction path modeling of albite dissolution in almost pure water at 25 °C (with a small amount of NaCl). The albite dissolution rate equation of Marty et al. (2015) was used for modeling. The use of different parameter values (e.g., surface area, rate constant) will generate different curves, but it remains that it takes a short period for a solution to reach the level of departure from the equilibrium of $> \Delta_r G = -40 \sim -60$ kJ/mol. (b) Reaction path modeling using the same parameters as in (a), but the Burch et al. (1993) rate law for $\Delta_r G$ dependence. The results show that it takes < 0.1 years for almost pure water to get off the second rate-plateau on left.

(Guo et al., 2020). For modeling weathering profiles, Maher et al. (2009) simulated a 226 ka chronosequence. In short, the $k_{+,1}$ rate plateau, parallel rate law, and a switch of mechanisms at far-from-equilibrium have little significance in geochemical models of the saturated zone.

The above results were from batch reactor calculations. Modeling open systems, e.g., using RTM, would give a longer time for solution chemistry to evolve toward equilibrium. However, this would not change the fact that it takes a short amount of time for a pure aqueous solution to react with feldspars and reach the $\Delta_r G > \Delta_r G_{crit}$ regions.

In short, dilute waters with $\Delta_r G < \Delta_r G_{crit}$ probably play an important role for a brief time in the unsaturated zone when rainfall replenishes the aquifer. The presence of etch pits on natural feldspars in some geological settings (Blum and Stillings, 1995; Zhu et al., 2006; Brantley, 2008) indicates a history of far-from-equilibrium dissolution or, more likely, acidic conditions aided by the presence of organic matters in soils and the $\Delta_r G_{crit}$ is more positive. These pre-existing etch pits could continue to operate in near-equilibrium dissolution (Lüttge, 2006; Luttge et al., 2019).

As pointed out by numerous authors, the parallel rate law of Eq. (4) is empirical. Zhu (2009) also pointed out the mathematical form of Eq. (4) does not constrain the parameters well; thousands of pairs of parameters can equally fit the experimental data. The slopes in these parallel rate laws were not well established, perhaps except for the Hellmann and Tisserand (2006) data. In order to fit the speculated slope, an $f(\Delta_r G)$ term was introduced in the first term on the RHS of Eq. (4). As pointed out by Zhu et al. (2020), this term implies albite precipitation at very far-from-equilibrium. This is theoretically unsound, particularly for experiments at $T < 100$ °C (Burch et al., 1993 at 80 °C; Taylor et al., 2000 at 25 °C), when the reverse reaction of feldspar precipitation probably did not happen even off the second rate plateau near-equilibrium.

In saturated geological media and when $T < 100$ °C, one can use $r+$ measured near-equilibrium in geochemical models (Zhu et al., 2020), which is equivalent to the $k_{+,2}$ term in Burch et al. (1993) and Hellmann and Tisserand (2006). The $k_{+,1}$ term is not significant in modeling as the system quickly passes that point, and therefore it can be ignored. For the unsaturated zone, a switch of mechanisms at far, far from equilibrium can be important. Each rainfall event will bring dilute water. Feldspars could dissolve in the very-far-from-equilibrium regime (−60 to –40 kJ/mol from albite saturation) for a short period of time. After this brief period and once $\Delta_r G$ becomes greater than $\Delta_r G_{crit}$, feldspar dissolution proceeds on the second-rate constant plateau, $k_{+,2}$. Luttge (2006) and Arvidson and Luttge (2010) suggested that this should be modeled as a two-step function, not the continuous parallel rate law of Eq. (4). At high temperatures (e.g., the experiments of Hellmann and Tisserand, 2006 at 150 °C), backward reaction of feldspar precipitation may occur, and the parallel rate law without the $f(\Delta_r G)$ term for the first plateau may be a good option.

6. CONCLUSIONS

It is extremely difficult to prepare a solution that is close to equilibrium to feldspars but not supersaturated with respect to many Al- and Si-phases. This is particularly true for near-neutral pH solutions. Therefore, near-equilibrium experimental data are scarce, and the limited data reported in the literature are restricted to highly acidic or alkaline conditions. Our study used the isotope tracer method and produced experimental data for albite dissolution at 50 °C and pH ~ 8 from $\Delta_r G$ of −26 to −2 kJ/mol from equilibrium. The r_+ values were nearly constant, suggesting no switch of $\Delta_r G$-related major reaction mechanisms within this $\Delta_r G$ range. The most plausible interpretation, after combining our rate data with far-from-equilibrium rates in the literature, is that the etch pit opening reaction mechanism, which was derived from experimental data under alkaline conditions, does not operate under circum-neutral pH (5–8).

Rate data from this study, together with the rates reported in Zhang (2019), showed that albite unidirectional dissolution rates are nearly constant in the pH range of 5–8, which supports the hypothesis of a water-catalyzed reaction mechanism. The water-catalyzed mechanism dominates in the circum-neutral pH region while the H^+- and OH^--catalysis reaction mechanisms dominate in the acid and alkaline pH regions, respectively. These findings lend support to the widely used kinetic rate compilations that are based on the three mechanism formulation (Palandri and Kharaka, 2004; Marty et al., 2015).

The Si isotope tracer experiments provided unidirectional dissolution rates (r_+) whereas previous studies of the relationship between rates and $\Delta_r G$ and rates and pH used the concentration-based experimental method and produced r_{net}. Measurements of r_+ values were successful even when Si- and Al-containing phase precipitation occurred, which allowed us to carry out experiments with Si, Al, and Na concentrations similar to the majority of surface and groundwater in nature. While the isotope tracer method overcomes some obstacles associated with the concentration-based method, near-equilibrium experiments remain challenging. The dissolved Al concentrations are difficult to determine and a tiny amount of secondary precipitates are difficult to identify. Recommended standard state thermodynamic properties may be for albite samples with different order–disorder. Both sources of uncertainty make pinpointing the equilibrium with albite difficult and the absolute values of calculated saturation indices suspect.

Experiments that attempt to establish how $\Delta_r G$ and pH influence rates and their underlying reaction mechanisms are still scarce. Many debates on reaction mechanisms in recent publications were based on a few experimental data points of known questionable quality. More experimental data are needed. The isotope tracer method now enables such many measurements that were not possible before. Direct measurements of near-equilibrium rates in solutions resembling natural water chemistry would be a promising venue to supply kinetic parameters for geochemical modeling.

Declaration of Competing Interest

The authors declare that they have no known competing financial interests or personal relationships that could have appeared to influence the work reported in this paper.

ACKNOWLEDGMENTS

First of all, we would like to acknowledge the pioneering and meticulous work on the rate versus Gibbs free energy of reaction relationships that we cited in the paper. Criticism of the experimental data does not detract from their significant historic contributions to geochemical kinetics. The authors are grateful to Jacques Schott for the discussion of experimental data and their interpretations. His insights and encyclopedia knowledge of geochemical kinetics and aqueous geochemistry resulted in better interpretations of the experimental results. We are also grateful to Huifang Xu and Hiromi Konishi for their valiant efforts to identify the secondary phases, Huifang Xu for XRD identification of albite, and Anne Hereford for editing. This article is dedicated to the memory of our co-author J. Don Rimstidt. Don passed away before this manuscript could be completed. He made a major contribution to this research, but sadly could not add his always valuable insights into the final manuscript and may not have agreed with all our conclusions. The review comments by three anonymous reviewers helped the clarity of the presentation in this paper.

This work was partially supported by the U.S. NSF grant EAR-1926734, the Faculty Research Support Program through the office of Vice Provost for Research at Indiana University, and the Haydn Murray chair endowment to CZ. Analysis of Si isotopes was funded to HLY by the State Key Laboratory of Continental Dynamics.

RESEARCH DATA

Research Data associated with this article can be accessed at http://hdl.handle.net/2022/25805.

APPENDIX A. SUPPLEMENTARY MATERIAL

Supplementary data to this article can be found online at https://doi.org/10.1016/j.gca.2021.03.023.

REFERENCES

Alekseyev V., Medvedeva L. and Bannykh L. (2004) Experimental and mathematical modeling of the kinetics of congruent and incongruent dissolution reactions of alkaline feldspars. *Geochem. Int. C/C of Geokhimiia* **42**, 848–861.

Alekseyev V. A., Medvedeva L. S., Prisyagina N. I., Meshalkin S. S. and Balabin A. I. (1997) Change in the dissolution rates of alkali feldspars as a result of secondary mineral precipitation and approach to equilibrium. *Geochim. Cosmochim. Acta* **61**, 1125–1142.

Arvidson R. S. and Luttge A. (2010) Mineral dissolution kinetics as a function of distance from equilibrium - New experimental results. *Chem. Geol.* **269**, 79–88.

Beig M. S. and Lüttge A. (2006) Albite dissolution kinetics as a function of distance from equilibrium: Implications for natural feldspar weathering. *Geochim. Cosmochim. Acta* **70**, 1402–1420.

Bennett P., Rogers J., Choi W. and Hiebert F. (2001) Silicates, silicate weathering, and microbial ecology. *Geomicrobiol J.* **18**, 3–19.

Berger G., Beaufort D. and Lacharpagne J. C. (2002) Experimental dissolution of sanidine under hydrothermal conditions: Mechanism and rate. *Am. J. Sci.* **302**, 663–685.

Blum A. E. and Lasaga A. C. (1991) The role of surface speciation in the dissolution of albite. *Geochim. Cosmochim. Acta* **55**, 2193–2201.

Blum A. E. and Stillings L. L. (1995) Feldspar dissolution kinetics. In *Chemical Weathering Rates of Silicate Minerals* (eds. A. F. White and S. L. Brantley). Mineralogical Society of America, pp. 291–346.

Brantley S. L. (2008) Kinetics of mineral dissolution. In *Kinetics of Water-Rock Interaction* (eds. S. L. Brantley, J. D. Kubicki and A. F. White). Springer, New York, pp. 151–210.

Brantley S. L., Kubicki J. D. and White A. F. (2008) *Kinetics of water-rock interaction*. Springer.

Braunauer S., Emmett P. H. and Teller E. (1938) Adsorption of gases in mutlimolecular layers. *J. Am. Chem. Soc.* **60**, 309–319.

Burch T. E., Nagy K. L. and Lasaga A. C. (1993) Free energy dependence of albite dissolution kinetics at 80° C and pH 8.8. *Chem. Geol.* **105**, 137–162.

Chen Y. and Brantley S. L. (1997) Temperature- and pH-dependence of albite dissolution rate at acid pH. *Chem. Geol.* **135**, 275–290.

Chou L. and Wollast R. (1984) Study of the weathering of albite at room temperature and pressure with a fluidized bed reactor. *Geochim. Cosmochim. Acta* **48**, 2205–2217.

Chou L. and Wollast R. (1985) Steady-state kinetics and dissolution mechanisms of albite. *Am. J. Sci.* **285**, 963–993.

Davis M. C., Wesolowski D. J., Rosenqvist J., Brantley S. L. and Mueller K. T. (2011) Solubility and near-equilibrium dissolution rates of quartz in dilute NaCl solutions at 398–473 K under alkaline conditions. *Geochim. Cosmochim. Acta* **75**, 401–415.

Devidal J.-L., Schott J. and Dandurand J.-L. (1997) An experimental study of kaolinite dissolution and precipitation kinetics as a function of chemical affinity and solution composition at 150°C, 40 bars, and pH 2, 6.8, and 7.8. *Geochim. Cosmochim. Acta* **61**, 5165–5186.

Dove P. M., Han N. and De Yoreo J. J. (2005) Mechanisms of classical crystal growth theory explain quartz and silicate dissolution behavior. *Proc. Natl. Acad. Sci.* **102**, 15357–15362.

Drever, J.I. (1988) The Geochemistry of Natural Waters: Surface and Groundwater Environment. Prentice-Hall, Englewood Cliffs, New Jersey.

Fischer C., Arvidson R. S. and Lüttge A. (2012) How predictable are dissolution rates of crystalline material?. *Geochim. Cosmochim. Acta* **98** 177–185.

Gaillardet J. (2008) Isotope geochemistry as a tool for deciphering kinetics of water-rock interaction. In *Kinetics of Water-Rock Interaction* (eds. S. L. Brantley, J. D. Kubicki and A. F. White). Springer, New York.

Ganor J., Lu P., Zheng Z. and Zhu C. (2007) Bridging the gap between laboratory measurements and field estimations of silicate weathering using simple calculations. *Environ. Geol.* **53**, 599–610.

Gautier J.-M., Oelkers E. H. and Schott J. (1994) Experimental study of K-feldspar dissolution rates as a function of chemical affinity at 150° C and pH 9. *Geochim. Cosmochim. Acta* **58**, 4549–4560.

Georg R. B., Reynolds B. C., Frank M. and Halliday A. N. (2006) New sample preparation techniques for the precise determination of the Si isotope composition of natural samples using MC-ICP-MS. *Chem. Geol.* **235**, 95–104.

Georg R. B., Zhu C., Reynolds B. C. and Halliday A. N. (2009) Stable silicon isotopes of groundwater, feldspars, and clay coatings in the Navajo Sandstone aquifer, Black Mesa, Arizona, USA. *Geochim. Cosmochim. Acta* **73**, 2229–2241.

Gong L., Rimstidt J., Zhang Y., Chen K. and Zhu C. (2019) Unidirectional kaolinite dissolution rates at near-equilibrium and near-neutral pH conditions. *Appl. Clay Sci.* **182** 105284.

Govett G. (1961) Critical factors in the colorimetric determination of silica. *Anal. Chim. Acta* **25**, 69–80.

Gruber C., Harlavan Y., Pousty D., Winkler D. and Ganor J. (2019) Enhanced chemical weathering of albite under seawater conditions and its potential effect on the Sr ocean budget. *Geochim. Cosmochim. Acta* **261**, 20–34.

Gruber C., Harpaz L., Zhu C., Bullen T. D. and Ganor J. (2013) A new approach for measuring dissolution rates of silicate minerals by using silicon isotopes. *Geochim. Cosmochim. Acta* **104**, 261–280.

Gruber C., Kutuzov I. and Ganor J. (2016) The combined effect of temperature and pH on albite dissolution rate under far-from-equilibrium conditions. *Geochim. Cosmochim. Acta* **186**, 154–167.

Gruber C., Zhu C., Georg R. B., Zakon Y. and Ganor J. (2014) Resolving the gap between laboratory and field rates of feldspar weathering. *Geochim. Cosmochim. Acta* **147**, 90–106.

Guo X. L., Gin S., Lei P. H., Yao T. K., Liu H. S., Schreiber D. K., Ngo D., Viswanathan G., Li T. S., Kim S. H., Vienna J. D., Ryan J. V., Du J. C., Lian J. and Frankel G. S. (2020) Self-accelerated corrosion of nuclear waste forms at material interfaces. *Nat. Mater.* **19**, 310-+.

Helgeson H. C., Delany J. M., Nesbitt H. W. and Bird D. K. (1978) Summary and critique of the thermodynamic properties of rock forming minerals. *Am. J. Sci.* **278A**, 569–592.

Helgeson H. C., Kirkham D. H. and Flowers G. C. (1981) Theoretical prediction of the thermodynamic behavior of aqueous electrolytes at high pressures and temperatures. IV. Calculation of activity coefficients, osmotic coefficients, and apparent molal and standard and relative partial molal properties to 600°C and 5 kb. *Am. J. Sci.* **281**, 1249–1516.

Hellmann R. (1994) The albite-water system; Part I, The kinetics of dissolution as a function of pH at 100, 200, and 300°C. *Geochim. Cosmochim. Acta* **58**, 595–611.

Hellmann R. and Tisserand D. (2006) Dissolution kinetics as a function of the Gibbs free energy of reaction: An experimental study based on albite feldspar. *Geochim. Cosmochim. Acta* **70**, 364–383.

Holdren G. R. and Berner R. A. (1979) Mechanism of feldspar weathering-I. Experimental studies. *Geochim. Cosmochim. Acta* **43**, 1161–1171.

Holland T. and Powell R. (2011) An improved and extended internally consistent thermodynamic dataset for phases of petrological interest, involving a new equation of state for solids. *J. Metamorph. Geol.* **29**, 333–383.

Johnson J. W., Oelkers E. H. and Helgeson H. C. (1992) SUPCRT92 - A software package for calculating the standard molal thermodynamic properties of minerals, gases, aqueous species, and reactions from 1-bar to 5000-bar and 0°C to 1000° C. *Comput. Geosci.* **18**, 899–947.

Knauss K. G. and Wolery T. J. (1986) Dependence of albite kinetics on pH and time at 25 °C and 70°C. *Geochim. Cosmochim. Acta* **50**, 2481–2497.

Langmuir, D. (1997) Aqueous Environmental Geochemistry. Prentice Hall, Upper Saddle River, New Jersey.

Lasaga A. C. (1998) *Kinetic Theory in the Earth Sciences*. Princeton University Press, Princeton, New Jersey.

Lasaga A. C., Soler J. M., Ganor J., Burch T. E. and Nagy K. L. (1994) Chemical weathering rate laws and global geochemical cycles. *Geochim. Cosmochim. Acta* **58**, 2361–2386.

Liu Z., Rimstidt J. D., Zhang Y. and Zhu C. (2016) A stable isotope doping method to test the range of applicability of detailed balance. *Geochem. Perspect. Lett.* **2**, 78–86.

Lu P., Fu Q., Seyfried, Jr., W. E., Hedges S. W., Soong Y., Jones K. and Zhu C. (2013) Coupled alkali feldspar dissolution and secondary mineral precipitation in batch systems: 2. New Experiments with Supercritical CO2 and Implications for Carbon Sequestration. *Appl. Geochem.* **30**, 75–90.

Lüttge A. (2006) Crystal dissolution kinetics and Gibbs free energy. *J. Electron Spectrosc. Relat. Phenom.* **150**, 248–259.

Luttge A., Arvidson R. S., Fischer C. and Kurganskaya I. (2019) Kinetic concepts for quantitative prediction of fluid-solid interactions. *Chem. Geol.* **504**, 216–235.

Maher K., Steefel C. I., White A. F. and Stonestrom D. A. (2009) The role of reaction affinity and seocndary mienrals in regulating chemical weathering rates at the Santa Cruz Soil Chronosequence. *California. Geochim. Cosmochim. Acta* **73**, 2804–2831.

Marini L. (2007) *Geological sequestration of carbon dioxide: thermodynamics, kinetics, and reaction path modeling*. Elsevier.

Marty N. C., Claret F., Lassin A., Tremosa J., Blanc P., Madé B., Giffaut E., Cochepin B. and Tournassat C. (2015) A database of dissolution and precipitation rates for clay-rocks minerals. *Appl. Geochem.* **55**, 108–118.

McBride M. B. (1994) *Environmental Chemistry of Soils*. Oxford University Press, New York.

Miron G. D., Wagner T., Kulik D. A. and Heinrich C. A. (2016) Internally consistent thermodynamic data for aqueous species in the system Na–K–Al–Si–O–H–Cl. *Geochim. Cosmochim. Acta* **187**, 41–78.

Oelkers E. H. and Gislason S. R. (2001) The mechanism, rates and consequences of basaltic glass dissolution: I. An experimental study of the dissolution rates of basaltic glass as a function of aqueous Al, Si and oxalic acid concentration at 25°C and pH=3 and 11. *Geochim. Cosmochim. Acta* **65**, 3671–3681.

Oelkers E. H. and Helgeson H. C. (1990) Triple-ion anions and polynuclear complexing in supercritical electrolyte-solutions. *Geochim. Cosmochim. Acta* **54**, 727–738.

Oelkers E. H. and Schott J. (1995) Experimental study of anorthite dissolution and the relative mechanism of feldspar hydrolysis. *Geochim. Cosmochim. Acta* **59**, 5039–5053.

Oelkers E. H. and Schott J. (1999) Experimental study of kyanite dissolution rates as a function of chemical affinity and solution composition. *Geochim. Cosmochim. Acta* **63**, 785–797.

Oelkers E. H., Schott J. and Devidal J. L. (1994) The effect of aluminum, pH, and chemical affinity on the rates of aluminosilicate dissolution reactions. *Geochim. Cosmochim. Acta* **58**, 2011–2024.

Oelkers, E.H., Schott, J. and Devidal, J.L. (2001) On the interpretation of closed system mineral dissolution experiments: Comment on "Mechanism of kaolinite dissolution at room temperature and pressure Part II: Kinetic study" by Huertas et al. (1999). Geochim. Cosmochim. Acta 65, 4429-4432.

Oelkers E. H., Schott J., Gauthier J.-M. and Herrero-Roncal T. (2008) An experimental study of the dissolution mechanism and rates of muscovite. *Geochim. Cosmochim. Acta* **72**, 4948–4961.

Palandri J. L. and Kharaka Y. K. (2004) A compilation of rate parameters of water-mineral interaction kinetics for application to geochemical modeling. *US Geological Survey, Open File Report*, 2004–11068.

Parkhurst D. L. and Appelo C. (2013) Description of input and examples for PHREEQC version 3—a computer program for speciation, batch-reaction, one-dimensional transport, and inverse geochemical calculations. *US geological survey techniques and methods, book* **6**, 497.

Pollet-Villard M., Daval D., Ackerer P., Saldi G. D., Wild B., Knauss K. G. and Fritz B. (2016) Does crystallographic anisotropy prevent the conventional treatment of aqueous mineral reactivity? A case study based on K-feldspar dissolution kinetics. *Geochim. Cosmochim. Acta* **190**, 294–308.

Rimstidt J. D. (1997) Quartz solubility at low temperatures. *Geochim. Cosmochim. Acta* **61**, 2553–2558.

Rimstidt J. D. (2014) *Geochemical Rate Models: An Introduction to Geochemical Kinetics*. Cambridge University Press.

Rose N. M. (1991) Dissolution Rates of Prehnite, Epidote and Albite. *Geochim. Cosmochim. Acta* **55**, 3273–3286.

Schott J., Oelkers E. H., Benezeth P., Godderis Y. and Francois L. (2012) Can accurate kinetic laws be created to describe chemical weathering? *C.R. Geosci.* **344**, 568–585.

Schweda P. (1990) Kinetics and mechanisms of alkali feldspar dissolution at low temperatures. In *Dept of Geology and Geochemistry*. Stockholm University, pp. 609–612.

Shock E. L. and Helgeson H. C. (1988) Calculation of the thermodynamic and transport properties of aqueous species at high pressures and temperatures: Correlation algorithms for ionic species and equation of state predictions to 5 kb and 1000° C. *Geochim. Cosmochim. Acta* **52**, 2009–2036.

Shock E. L., Helgeson H. C. and Sverjensky D. A. (1989) Calculations of the thermodynamic and transport properties of aqueous species at high pressures and temperatures: Standard partial molal properties of inorganic neutral species. *Geochim. Cosmochim. Acta* **53**, 2157–2183.

Shock E. L., Sassani D. C., Willis M. and Sverjensky D. A. (1997) Inorganic species in geologic fluids: Correlations among standard molal thermodynamic properties of aqueous ions and hydroxide complexes. *Geochim. Cosmochim. Acta* **61**, 907–950.

Siivola, J. and Schmid, R. (2007) List of Mineral Abbreviations. web site.

Stefansson A. (2001) Dissolution of primary minerals of basalt in natural waters: I. Calculation of mineral solubilities from 0 C to 350 C. *Chem. Geol.* **172**, 225–250.

Stefansson A. and Gislason S. R. (2001) Chemical weathering of basalts, Southwest Iceland: Effect of rock crystallinity and

secondary minerals on chemical fluxes to the ocean. *Am. J. Sci.* **301**, 513–556.

Stillings L. L. and Brantley S. L. (1995) Feldspar dissolution at 25° C and pH 3: reaction stoichiometry and the effect of cations. *Geochim. Cosmochim. Acta* **59**, 1483–1496.

Stumm W. (1992) *Chemistry of Solid-Water Interfaces: processes at the mineral-water and particle-water interface in natural systems*, 1st ed. John Wiley & Sons, New York.

Su C. and Harsh J. B. (1994) Gibbs free energies of formation at 298 K for imogolite and gibbsite from solubility measurements. *Geochim. Cosmochim. Acta* **58**, 1667–1677.

Su C. M. and Harsh J. B. (1998) Dissolution of allophane as a thermodynamically unstable solid in the presence of boehmite at elevated temperatures and equilibrium vapor pressures. *Soil Sci.* **163**, 299–312.

Sverjensky D. A., Shock E. L. and Helgeson H. C. (1997) Prediction of the thermodynamic properties of aqueous metal complexes to 1000 °C and 5 Kb. *Geochim. Cosmochim. Acta* **61**, 1359–1412.

Tagirov B. and Schott J. (2001) Aluminum speciation in crustal fluids revisited. *Geochim. Cosmochim. Acta* **65**, 3965–3992.

Tanger J. C. and Helgeson H. C. (1988) Calculations of the thermodynamic and transport properties of aqueous species at high pressures and temperatures: Revised equation of state for the standard partial molal properties of ions and electrolytes. *Am. J. Sci.* **288**, 19–98.

Taylor A. S., Blum J. D. and Lasaga A. C. (2000) The dependence of labradorite dissolution and Sr isotope release rates on solution saturation state. *Geochim. Cosmochim. Acta* **64**, 2389–2400.

Tutolo B. M., Kong X.-Z., Seyfried, Jr., W. E. and Saar M. O. (2014) Internal consistency in aqueous geochemical data revisited: Applications to the aluminum system. *Geochim. Cosmochim. Acta* **133**, 216–234.

White A. F. (1995) Chemical weathering of silicate minerals in soils. In *Chemical Weathering Rates of Silicate Minerals* (eds. A. F. White and S. L. Brantley). Mineralogical Society of America, pp. 407–458.

White A. F. and Brantley S. L. (1995) Chemical weathering rates of silicate minerals: an overview. *Chem. Weathering Rates of Silicate Miner.* **31**, 1–22.

Wieland E., Wehrli B. and Stumm W. (1986) The coordination chemistry of weathering: III. A generalization on the dissolution rates of minerals. *Geochim. Cosmochim. Acta* **52**, 1969–1981.

Yuan H., Cheng C., Chen K. and Bao Z. (2016) Standard-sample bracketing calibration method combined with Mg as an internal standard for silicon isotopic compositions using multi-collector inductively coupled plasma mass spectrometry. *Acta Geochim.* **35**, 421–427.

Zhang Y. (2018) *An experimental and modeling study of slicate dissolution kinetics near equilibrium*. Indiana University, p. 351.

Zhang Y. (2019) *An experimental and modeling study of silicate mineral dissolution kinetics near equilibrium*. Indiana University, p. 102.

Zhang Y., Hu B., Teng Y. and Zhu C. (2019) A library of BASIC scripts of rate equations for geochemical modeling using PHREEQC. *Comput. Geosci.*.

Zhu C. (2009) Geochemical modeling of reaction paths and geochemical reaction networks. In *Thermodynamics and Kinetics of Water-Rock Interaction* (eds. E. H. Oelkers and J. Schott). Mineralogical Society of America, pp. 533–569.

Zhu C., Liu Z., Zhang Y., Wang C., Scheafer A., Lu P., Zhang G., Georg R. B., Yuan H. and Rimstidt J. D. (2016) Measuring silicate mineral dissolution rates using Si isotope doping. *Chem. Geol.* **445**, 145–163.

Zhu C. and Lu P. (2009) Alkali feldspar dissolution and secondary mineral precipitation in batch systems: 3. Saturation states of product minerals and reaction paths. *Geochim. Cosmochim. Acta* **73**, 3171–3200.

Zhu C., Lu P., Zheng Z. and Ganor J. (2010) Coupled alkali feldspar dissolution and secondary mineral precipitation in batch systems: 4. Numerical modeling of kinetic reaction paths. *Geochim. Cosmochim. Acta* **74**, 3963–3983.

Zhu C., Rimstidt J. D., Zhang Y. L., Kang J. T., Schott J. and Yuan H. L. (2020) Decoupling feldspar dissolution and precipitation rates at near-equilibrium with Si isotope tracers: Implications for modeling silicate weathering. *Geochim. Cosmochim. Acta* **271**, 132–153.

Zhu C., Veblen D. R., Blum A. E. and Chipera S. J. (2006) Naturally weathered feldspar surfaces in the Navajo Sandstone aquifer, Black Mesa, Arizona: Electron microscopic characterization. *Geochim. Cosmochim. Acta* **70**, 4600–4616.

Zhu C., Zhang G., Lu P., Meng L. and Ji X. (2015) Benchmark modeling of the Sleipner CO2 plume: Calibration to seismic data for the uppermost layer and model sensitivity analysis. *Int. J. Greenhouse Gas Control* **43**, 233–246.

Zimmer, K., Zhang, Y., Lu, P., Chen, Y., Zhang, G., Dalkilic, M., Zhu, C., 2016. SUPCRTBL: A revised and extended thermodynamic dataset and software package of SUPCRT92. Comput. Geosci. 90, Part A, 97-111.

Associate editor: Carl Steefel